

Optimized Separation of Acetylene from Carbon Dioxide and Ethylene in a Microporous Material

Rui-Biao Lin,[†] Libo Li,^{†,§} Hui Wu,[‡] Hadi Arman,[†] Bin Li,[†] Rong-Guang Lin,^{†,||} Wei Zhou,^{*,‡} and Banglin Chen^{*,†}

[†]Department of Chemistry, University of Texas at San Antonio, One UTSA Circle, San Antonio, Texas 78249-0698, United States

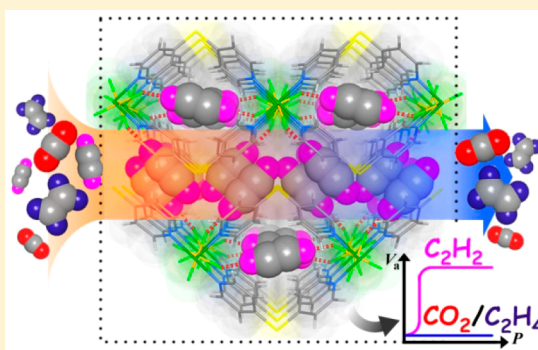
[‡]NIST Center for Neutron Research, National Institute of Standards and Technology, Gaithersburg, Maryland 20899-6102, United States

[§]Research Institute of Special Chemicals, Taiyuan University of Technology, Taiyuan 030024, Shanxi, China

^{||}School of Life Sciences, Fujian Agriculture and Forestry University, Fuzhou 350002, China

S Supporting Information

ABSTRACT: Selective separation of acetylene (C_2H_2) from carbon dioxide (CO_2) or ethylene (C_2H_4) needs specific porous materials whose pores can realize sieving effects while pore surfaces can differentiate their recognitions for these molecules of similar molecular sizes and physical properties. We report a microporous material $[Zn(dps)_2(SiF_6)]$ (UTSA-300, dps = 4,4'-dipyridylsulfide) with two-dimensional channels of about 3.3 Å, well-matched for the molecular sizes of C_2H_2 . After activation, the network was transformed to its closed-pore phase, UTSA-300a, with dispersed 0D cavities, accompanied by conformation change of the pyridyl ligand and rotation of SiF_6^{2-} pillars. Strong C–H...F and π – π stacking interactions are found in closed-pore UTSA-300a, resulting in shrinkage of the structure. Interestingly, UTSA-300a takes up quite a large amounts of acetylene ($76.4\text{ cm}^3\text{ g}^{-1}$), while showing complete C_2H_4 and CO_2 exclusion from C_2H_2 under ambient conditions. Neutron powder diffraction and molecular modeling studies clearly reveal that a C_2H_2 molecule primarily binds to two hexafluorosilicate F atoms in a head-on orientation, breaking the original intranetwork hydrogen bond and subsequently expanding to open-pore structure. Crystal structures, gas sorption isotherms, molecular modeling, experimental breakthrough experiment, and selectivity calculation comprehensively demonstrated this unique metal–organic framework material for highly selective C_2H_2/CO_2 and C_2H_2/C_2H_4 separation.



■ INTRODUCTION

Hydrocarbon separations are very important industrial processes providing several essential feedstocks for chemical transformations. Among them, acetylene (C_2H_2) is an important source of organic chemicals including acrylic acid derivatives, vinyl compounds, and α -ethynyl alcohols in the chemical industry.¹ C_2H_2 is mainly manufactured by the partial combustion of methane or comes from cracking of hydrocarbons, coexisting with carbon dioxide (CO_2) or ethylene (C_2H_4). However, the similarities between these molecules in terms of their molecular sizes, shapes ($3.32 \times 3.34 \times 5.7\text{ Å}^3$ for C_2H_2 , $3.18 \times 3.33 \times 5.36\text{ Å}^3$ for CO_2),² and physical properties (boiling points of 189.3 and 194.7 K for C_2H_2 and CO_2 , respectively) make C_2H_2 separation a great challenge. Compared with solvent extraction or cryogenic distillation, adsorptive separation using porous materials is more environmentally friendly and energy efficient and considered as a promising future separation technology.

As a new generation of porous materials, metal–organic frameworks (MOFs) and/or porous coordination polymers

(PCPs)³ have diverse applications in gas storage,⁴ separation,⁵ sensing,⁶ catalysis,⁷ drug delivery,⁸ and bioimaging,⁹ because of their unique pore structures and surfaces.¹⁰ The rational combination of metal ions/metal clusters of specific coordination geometries and organic ligands of fixed shapes has enabled us not only to design and synthesize porous MOFs of predictable topologies but also to control the pore sizes systematically to induce their different host–guest interactions/recognitions.¹¹ Benefiting from exquisite control over pore accessibility and pore surface, MOFs show great potential in the realm of C_2H_2 separation. For example, systematic tuning of pore geometry and chemistry provided SIFSIX materials with high adsorption capacity and selectivity for separation of C_2H_2/C_2H_4 mixtures.¹²

Ideal porous materials for gas separation are those with suitable pore sizes and geometries for complete size–shape sieving, so they only take up smaller molecules while

Received: April 16, 2017

Published: June 2, 2017

completely blocking the larger ones. Though porous MOF materials can be typically realized to exhibit certain sieving effects,¹³ very few have been targeted to exhibit complete exclusion of one molecule from the other components based on their size or shape differences,¹⁴ as demonstrated in the separation of branched paraffins from linear paraffins¹⁵ and propane from propylene.¹⁶ When the separating gas molecules have almost identical size and shape and similar physical properties, for example, C_2H_2/CO_2 , the complete exclusion of one component over another becomes very challenging.¹⁷ In fact, most reported MOFs show very similar uptake capacity and/or binding affinity for C_2H_2 and CO_2 ,¹⁸ whereas only very few reported porous materials for the separation of C_2H_2/CO_2 can fulfill partial sieving effect but no exclusive separation.¹⁹ In order to develop microporous materials for complete sieving effects for such a challenging separation, we need to not only fine-tune the pore sizes to match the molecular sizes of these two gas molecules of about 3.3 Å but also introduce some specific sites to bind C_2H_2 molecules exclusively, which has not been revealed yet in the literature.

During our exploration on ultramicroporous MOF materials, we discovered a novel SIFSIX-MOF, $[Zn(dps)_2(SiF_6)]$ (dps = 4,4'-dipyridylsulfide; termed as **UTSA-300**) with multiple potential binding sites and a pore aperture size of about 3.3 Å, which motivated us to examine its potential for gas separations. **UTSA-300** exhibits a pore open-close transformation during activation/desolvation, leading to a closed-pore framework **UTSA-300a** locked by multiple hydrogen bonds. Gas sorption studies indicate that **UTSA-300a** takes up quite a large amount of acetylene of $76.4\text{ cm}^3\text{ g}^{-1}$ but negligible amounts of carbon dioxide and ethylene under ambient conditions. Direct crystallography results reveal that the anisotropic adsorption site only allows C_2H_2 to open the pore structure by forming strong host–guest interactions in a head-on orientation. As a result, **UTSA-300a** can have complete CO_2 and C_2H_4 exclusion from the mixtures of C_2H_2/CO_2 and C_2H_2/C_2H_4 under ambient conditions, which can serve as a superior porous adsorbent for the challenging separation of C_2H_2/CO_2 and C_2H_2/C_2H_4 . Molecular modeling studies and experimental breakthroughs have exclusively supported the claim.

■ EXPERIMENTAL SECTION

Materials and Physical Measurements. All reagents and solvents were commercially available and directly used without further purification. Thermogravimetric analysis (TGA) was carried out under an argon atmosphere from room temperature to 900 °C using a Shimadzu TGA-50 analyzer at a heating rate of 10 °C min⁻¹. Powder X-ray diffraction (PXRD) patterns were collected using a Rigaku Ultima IV diffractometer (Cu K α) at 40 kV and 44 mA with a scan rate of 8.0°/min. The Fourier transform infrared (FT-IR) spectrum was obtained on a Nicolet iS50 FT-IR spectrometer (Thermo Scientific) at room temperature.

The gas sorption isotherms were collected on an automatic volumetric adsorption apparatus (Micromeritics ASAP 2020 surface area analyzer). Prior to the sorption measurements, the as-synthesized sample was exchanged with methanol six times and placed in a quartz tube and dried for 24 h at room temperature to remove the remnant solvent molecules, giving the activated **UTSA-300** for gas sorption analyses. To maintain the experimental temperatures, acetone–dry ice bath (195 K), ice–water bath (273 K), and water bath (298 K) were used.

Synthesis of $UTSA-300\cdot H_2O$. A methanol (10 mL) solution of $ZnSiF_6\cdot xH_2O$ (0.4 mmol, 82.8 mg) was poured into a methanol solution of dps (0.8 mmol, 150.6 mg) in a 20 mL vial and kept

undisturbed at room temperature for 12 h. Then pale yellow block crystals were collected, exchanged with methanol, and dried under vacuum, with yields of 67% based on Zn. Anal. Calcd (%) for $C_{20}H_{24}N_4O_4F_6Si_2Zn$ ($[Zn(dps)_2(SiF_6)]\cdot 4H_2O$): C, 36.6; H, 3.7; N, 8.5. Found: C, 36.8; H, 3.5; N, 8.5. IR (cm⁻¹): 3534 (m), 3423 (br, m), 3095 (w), 3040 (w), 1651 (w), 1601 (s), 1592 (vs), 1542 (m), 1490 (s), 1420 (s), 1328 (w), 1228 (m), 1217 (m), 1104 (w), 1065 (s), 1020 (s), 875 (w), 831 (vs).

X-ray and Neutron Crystallography. Single-crystal X-ray diffraction data of $UTSA-300\cdot H_2O$ were collected at 100(2) K using a Rigaku AFC12/Saturn 724 CCD fitted with Mo K α radiation ($\lambda = 0.71073$ Å). Data collection and unit cell refinement were conducted using Crystal Clear software.²⁰ Data processing and absorption correction were performed using Crystal Clear and ABCOR,²¹ respectively, to generate minimum and maximum transmission factors. The structure of $UTSA-300\cdot H_2O$ was solved using direct methods and refined on F^2 by full-matrix least-squares techniques using SHELXL.²² Except for solvent molecules, all non-hydrogen atoms were refined with anisotropic displacement parameters. All hydrogen atom positions were added to their mother carbon atoms by geometry and refined by a riding model.

Powder neutron diffraction data were collected using the BT-1 neutron powder diffractometer at the National Institute of Standards and Technology (NIST) Center for Neutron Research. A Ge(311) monochromator with a 75° takeoff angle, $\lambda = 2.0787(2)$ Å, and in-pile collimation of 60 min of arc was used. Data were collected over the range of 3–166.3° (2θ) with a step size of 0.05°. Fully activated **UTSA-300a** sample was loaded in a vanadium can equipped with a capillary gas line and a packless valve. A closed-cycle He refrigerator was used for sample temperature control. The activated **UTSA-300a** sample was measured first at the temperature of 296 K. To probe the acetylene adsorption locations, C_2D_2 (note that deuterated acetylene was used because H has large incoherent neutron scattering cross section and thus would introduce large background in the diffraction data) was loaded into the sample at room temperature, and diffraction data were then collected on the C_2D_2 -loaded MOF samples.

Rietveld structural refinement was performed on the neutron diffraction data using the GSAS package.²³ Due to the large number of atoms in the crystal unit cell, the ligand molecule and the gas molecule were both treated as rigid bodies during the Rietveld refinement, with the molecule orientation and center of mass freely refined. Final refinement on the positions/orientations of the rigid bodies, thermal factors, occupancies, lattice parameters, background, and profiles converges with satisfactory R factors.

Crystallographic data and refinement information are summarized in Table S1. CCDC 1542453–1542455 contain the supplementary crystallographic data of $UTSA-300\cdot H_2O$, $UTSA-300\cdot C_2D_2$, and **UTSA-300a**, respectively. These data can be obtained free of charge from the Cambridge Crystallographic Data Centre via www.ccdc.cam.ac.uk/data_request/cif.

Density Functional Theory Calculations. First-principles density functional theory (DFT) calculations were performed using the Quantum-Espresso package.²⁴ A semiempirical addition of dispersive forces to conventional DFT was included in the calculation to account for van der Waals interactions.²⁵ We used Vanderbilt-type ultrasoft pseudopotentials and generalized gradient approximation (GGA) with a Perdew–Burke–Ernzerhof (PBE) exchange correlation. A cutoff energy of 544 eV and a $2 \times 2 \times 2$ k-point mesh (generated using the Monkhorst–Pack scheme) were found to be enough for the total energy to converge within 0.01 meV/atom. We first optimized the structure of open-pore **UTSA-300**. C_2H_2 gas molecule was then introduced to the optimized host structure at the experimentally identified adsorption site, followed by a full structural relaxation. To obtain the gas binding energy, an isolated gas molecule placed in a supercell (with the same cell dimensions as the MOF crystal) was also relaxed as a reference. The static binding energy (at $T = 0$ K) was then calculated using $E_B = E(\text{MOF}) + E(C_2H_2) - E(\text{MOF} + C_2H_2)$.

RESULTS AND DISCUSSION

Reaction of 4,4'-dipyridylsulfide (dps) with ZnSiF_6 in methanol at room temperature yielded pale yellowish block-shaped crystals of $[\text{Zn}(\text{dps})_2(\text{SiF}_6)] \cdot 6\text{H}_2\text{O}$ (UTSA-300) (Figure 1a and

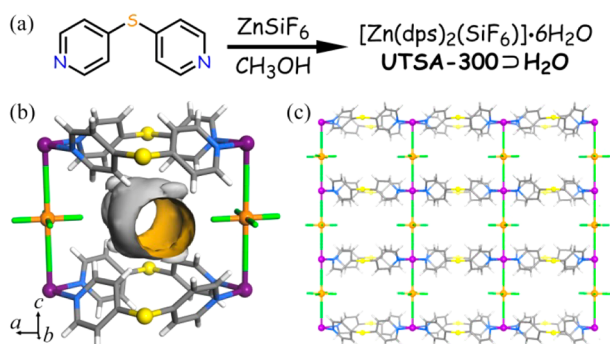


Figure 1. (a) Schematic synthesis of $\text{UTSA-300} \cdot 6\text{H}_2\text{O}$, (b) perspective views of cage unit (Zn, Si, F, S, N, and C are represented by purple, orange, green, bright yellow, light blue, and gray, respectively, and solvent molecules are omitted for clarity) and (c) coordination layer in UTSA-300 .

Supporting Information Figure S1). Single-crystal X-ray diffraction reveals that $\text{UTSA-300} \cdot 6\text{H}_2\text{O}$ crystallizes in orthorhombic $Ibam$ space group and exhibits a two-dimensional pore channel. There are one Zn(II) atom (1/4 occupancy), one-quarter of a SiF_6^{2-} group, one-half of a dps ligand, and one and half guest water molecules in the asymmetric unit of $\text{UTSA-300} \cdot 6\text{H}_2\text{O}$ (Figure S2). Each Zn(II) center is coordinated octahedrally by four pyridyl N atoms from four

different dps ligands and two F atoms from two different hexafluorosilicate. All the organic ligands and SiF_6^{2-} groups are two-connected with Zn(II) atoms. Each dps ligand exhibits a typical twisted conformation, with the dihedral angle between the planes of two pyridyl rings of $79.65(5)^\circ$. Each Zn(II) atom is expanded to four adjacent Zn(II) atoms via two pairs of double-stranded dps bridges and two hexafluorosilicates, forming a pseudocubic-like cavity (Figure 1b). The interconnection of adjacent Zn atoms gives a wavy-layered network, which can be considered as the connection of infinite pseudocubic cavities via edge-sharing and face-sharing. Regarding the Zn atoms as four-connected nodes and the ligands as linkers, the network topology of UTSA-300 can be simplified as **sql**. The layered structures are further connected by multiple interlayer hydrogen bonds between guest water molecules and free hexafluorosilicate F atoms ($\text{F} \cdots \text{O}$ 2.753(1)–2.801(1) Å). The removal of water molecules might cause structural transformation as these interactions would disappear. Without consideration of these guest molecules, UTSA-300 has undulating 2D channels (void = 29.3%) across the ab -plane (Figure 1c), being different from typical SIFSIX materials, which usually have accessible one-dimensional channels along the metal hexafluorosilicate chains (z coordination axis).²⁶ This difference can be attributed to the conformation of dps ligand and steric hindrance, resulting in the tilting of coordinated pyridyl rings (dihedral angle: $70.66(5)^\circ$) and rotation of SiF_6^{2-} (Figure S3), thus further reducing the pore size of UTSA-300 . The cavity sizes in UTSA-300 are $4.3 \times 4.3 \times 4.1$ and $3.5 \times 3.9 \times 4.1 \text{ Å}^3$, and the apertures are about $2.4 \times 3.3 \text{ Å}^2$ (Figure S4), which is smaller than $4.5 \times 4.5 \text{ Å}^2$ for SIFSIX-3-Zn²⁷ and matches well with the molecular size of C_2H_2 and CO_2 ,

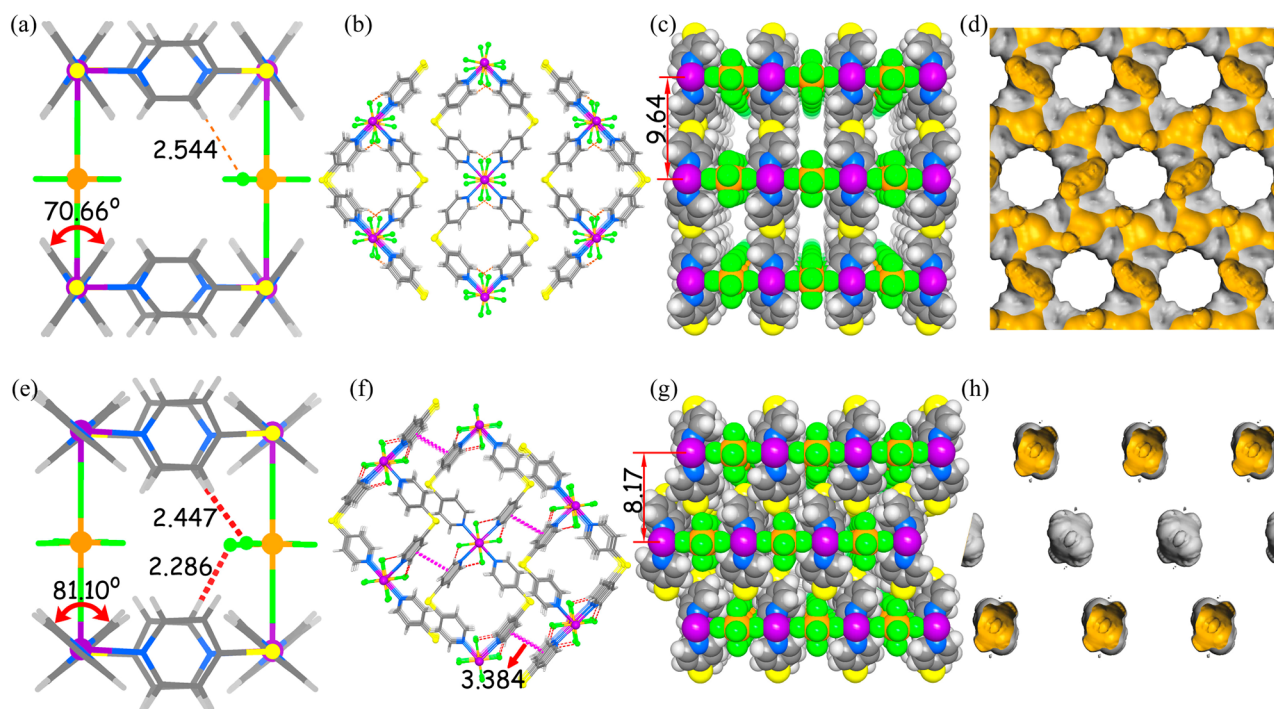


Figure 2. Comparison of crystal structures and channel shapes between $\text{UTSA-300} \cdot 6\text{H}_2\text{O}$ (a–d) and dense UTSA-300a (e–h); Zn, Si, F, S, N, and C are represented by purple, orange, green, bright yellow, light blue, and gray, respectively, and solvent molecules are omitted for clarity. (a,e) Perspective views of cage units in both structures, showing the tilting of pyridyl ring and C–H \cdots F interactions with highlight of angles and distances. (b,f) Top and (c,g) side views of both packing diagram with highlighted C–H \cdots F (red), π – π (pink) interactions, and the shrinkage of interlayer distance. (d,h) Calculated pore surface.

underlying size sieving for the potential separation of these gases.

The purity of the bulk products was confirmed by comparison of the simulated and experimental PXRD patterns (Figure S5) and further supported by elemental analysis and thermogravimetric analysis. TGA reveals that **UTSA-300** D_2O lost all guest water molecules at 120–130 °C with a weight loss of 14.9% (Figure S6), consistent with theoretical value (15.6%) from X-ray crystallography. We found that the guest molecules in **UTSA-300** D_2O can also be easily removed at room temperature under high vacuum, which gave an activated phase of **UTSA-300a** showing a different PXRD pattern with obvious shifts from the as-synthesized one (Figure S5). Though dramatic structural transformation during the activation of **UTSA-300** makes it impossible to maintain single-crystallinity, we were still able to solve and locate the atoms from the low quality single-crystal data (Figure S7). Fortunately, based on this structural model, the guest-free structure **UTSA-300a** was successfully solved by Rietveld refinement from high-quality neutron powder diffraction (NPD) data (Figure S8). Crystallography analyses reveal that the space group changes from *Ibam* (No. 72) to *P2₁/n* (No. 13) during the phase transformation. A shrinkage of the network with interlayer distance decreasing from 9.64 to 8.17 Å was observed, although the coordination modes and connections between metal nodes and linkers are the same as the as-synthesized one (Figure 2). Significantly, compared to the synthesized structure, stronger hydrogen bonding between one pyridyl ring of the dps ligand and all F atoms of SiF_6^{2-} ($\text{H}\cdots\text{F}$ 2.286–2.447 Å, $\text{C}-\text{H}\cdots\text{F}$ 3.214–3.370 Å) formed, accompanied by a larger tilting of the other pyridyl ring and rotation of SiF_6^{2-} (Figure 2a,e). It should be noted that here are two configurations of SiF_6^{2-} groups in the as-synthesized structure. However, after guest removal, all SiF_6^{2-} groups rotated to only one configuration, showing complete overlap from top view of the ZnSiF_6 chain (Figure 2b,f). Thus, the crystallographic axis along the ZnSiF_6 chain in guest-free **UTSA-300a** is only one-half of the as-synthesized one, as the rotation of its SiF_6^{2-} group is restricted. The dps ligand exhibits a more twisted conformation (the dihedral angle between two pyridyl planes is 86.44°), thus blocking all the apertures of the pseudocubic cavity. The conformation change of the ligand allows the formation of interlayer $\pi-\pi$ stacking (Figure 2f), giving a dense structure (closed-pore phase, **UTSA-300-cp**) with dispersed 0D cavities ($2.6 \times 3.9 \times 4.3 \text{ Å}^3$, void = 14.7%, Figures 2h and S9). Detailed comparison of the calculated pore size distributions (PSD) also shows that the distribution at around 3.3 Å disappears in closed-pore **UTSA-300a** (Figure S10), corresponding to the aperture blocking, which highlights the potential of using selective gate effect for separation. PXRD pattern shows that **UTSA-300a** is stable in air (Figure S11).

The porosity of **UTSA-300a** was first checked by N_2 (77 K) and CO_2 (195 K) adsorption (Figure 3a). For N_2 , no appreciable adsorption could be observed due to the large kinetic diameter of N_2 (3.64 Å) compared to the aperture size (3.3 Å). In contrast, the CO_2 sorption isotherms exhibit stepwise type (around $P/P_0 = 0.08$) with a hysteresis, which can be attributed to molecular clustering followed by pore filling, suggesting **UTSA-300a** can be expanded to open-pore state. **UTSA-300a** has a BET surface area of 311 m^2/g (Langmuir surface area of 444 m^2/g) and a total pore volume of 0.16 $\text{cm}^3 \text{g}^{-1}$ (Figure S12). This measured pore volume is obviously higher than that of the closed-pore **UTSA-300a** (calculated to

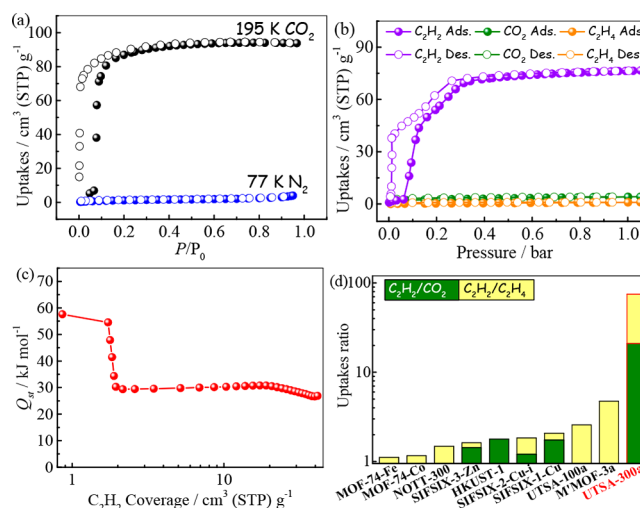


Figure 3. (a) Low-temperature N_2 and CO_2 sorption isotherms for **UTSA-300a**. (b) C_2H_2 , CO_2 , and C_2H_4 sorption isotherms for **UTSA-300a** at 273 K. (c) Adsorption enthalpies of C_2H_2 . (d) Comparison of uptakes ratio among representative MOFs.

be 0.09 $\text{cm}^3 \text{g}^{-1}$) but slightly lower than the as-synthesized one of 0.22 $\text{cm}^3 \text{g}^{-1}$, suggesting the pore opening during gas adsorption, and there are some small pores that are inaccessible for CO_2 (Figure S10), which matches with the corresponding structure.

The unique pore chemistry and pore geometry associated with suitable pore aperture size (about 3.3 Å) prompted us to evaluate the C_2H_2 and CO_2 adsorption performance of **UTSA-300a**. Hence, low-pressure C_2H_2 , CO_2 , and C_2H_4 sorption data from 273 to 298 K were collected (Figures 3b and S13). As expected, **UTSA-300a** takes up a large amount of C_2H_2 (3.41 mmol g^{-1} , 76.4 $\text{cm}^3 \text{g}^{-1}$) at 1 bar and 273 K, which is comparable to 3.86 mmol g^{-1} (86.4 $\text{cm}^3 \text{cm}^{-3}$) in SIFSIX-3-Zn.¹² However, to our big surprise, **UTSA-300a** adsorbs negligible amounts of CO_2 (0.18 mmol g^{-1} , 4.1 $\text{cm}^3 \text{g}^{-1}$) and C_2H_4 (0.04 mmol g^{-1} , 0.92 $\text{cm}^3 \text{g}^{-1}$) at the same condition, which is less than any other MOF materials with considerable uptake of C_2H_2 .^{12,19a,26,28} Compared with other MOFs,^{12,19a,28,29} the uptake ratios of $\text{C}_2\text{H}_2/\text{CO}_2$ and $\text{C}_2\text{H}_2/\text{C}_2\text{H}_4$ for **UTSA-300a** at 1 bar are very high and up to 19 and 83 (Figure 3d and Table S2), suggesting potential application to address the challenging separation of these gases under ambient condition. Further, no obvious C_2H_4 uptake can be observed even at 195 K (Figure S14). Therefore, for the insufficient C_2H_4 adsorption, it can be attributed to complete size exclusion because its kinetic diameter (4.2 Å) is obviously larger than the aperture size of **UTSA-300** (3.3 Å) rather than structural flexibility.³⁰ However, the significantly different adsorption behavior for C_2H_2 and CO_2 under ambient conditions is really unusual considering their identical kinetic diameters (3.3 Å). Multiple sorption measurements were consequently conducted carefully, and nothing different but the same result was found (Figures S15–S20).

To structurally understand the unique sorption behavior, we performed high-resolution NPD measurements to establish the structure of the C_2H_2 binding sites. Considering the flexibility implied by the stepwise sorption isotherms, NPD data of **UTSA-300** C_2D_2 were collected at room temperature on two different C_2D_2 -loaded samples. After C_2D_2 loading, the diffraction pattern (particularly peak positions) changed

dramatically (Figure S21), suggesting that adsorption induced a significant structural transformation of the host framework. Due to the asynchronous and/or incomplete transformation, it is difficult to get the intermediate structure from the low C_2D_2 loading data as it cannot be indexed to a single phase (Figures S21 and S22). Fortunately, the structure of $\text{UTSA-300} \supset \text{C}_2\text{D}_2$ can be well-defined from high-quality NPD data of high-loading $[\text{Zn}(\text{dps})_2(\text{SiF}_6)] \cdot 3.57\text{C}_2\text{D}_2$ (Figure 4 and Figures S23 and

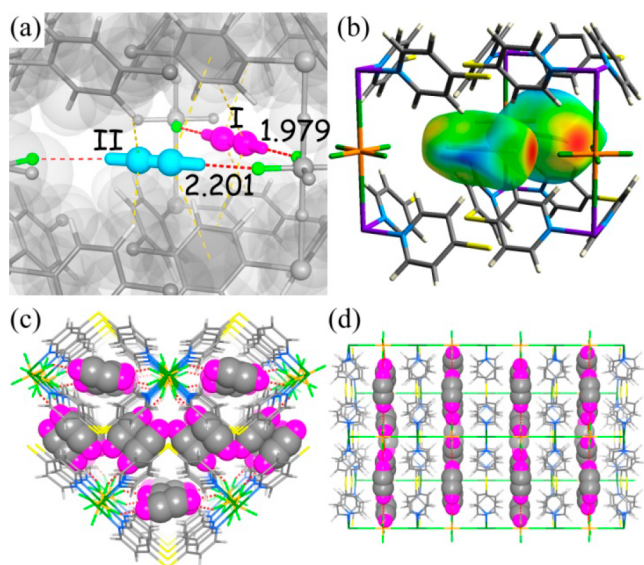


Figure 4. Neutron diffraction crystal structure of $\text{UTSA-300} \supset \text{C}_2\text{D}_2$ showing (a) preferential binding sites for C_2D_2 molecules (sites I and II) and their close contacts with the framework. (b) Hirshfeld surface (d_i) displaying $\text{C}-\text{D} \cdots \text{F}$ interactions (red area). (c,d) Top and side views of C_2D_2 adsorbed packing diagram; C_2D_2 molecules are shown in a CPK model.

S24). Detailed comparison reveals that the crystal symmetry changes back to *Ibam*, and the coordination network is fully restored to its original state (open-pore phase, UTSA-300-op) of the as-synthesized structure, which implies the pore is opened by C_2D_2 . With the help of Fourier difference analysis and Rietveld refinements, the C_2D_2 binding sites were successfully located in $\text{UTSA-300} \supset \text{C}_2\text{D}_2$. Two C_2D_2 binding sites can be identified from the data (denoted as sites I and II), as shown in Figure 4a. The C_2D_2 occupancies were determined by free structural refinement to be 0.87(1) and 0.461(8) at sites I and II, respectively. In open-pore UTSA-300 , dispersed C_2D_2 molecules are bound through strong $\text{C}-\text{D} \cdots \text{F}$ hydrogen bonding and van der Waals (vdW) interactions with the pyridyl rings of the dps ligand, the same as the acetylene binding in SIFSIX MOFs.¹² On site I, located inside the pseudocubic cavity, the only C_2D_2 molecule is symmetrically bound to two terminal F atoms of different SiF_6^{2-} units ($\text{D} \cdots \text{F}$ 1.979(27) Å, $\text{C}-\text{D} \cdots \text{F}$ 3.039(29) Å), accompanied by multiple vdW interactions between C_2D_2 and the pyridyl rings (3.775(24) Å) (Figure 4b). In contrast, on site II, the C_2D_2 molecule is asymmetrically bound to one close F atom ($\text{D} \cdots \text{F}$ 2.201(37) Å, $\text{C}-\text{D} \cdots \text{F}$ 3.281(37) Å) together with a weaker interaction with another F atom ($\text{D} \cdots \text{F}$ 2.895(38) Å, $\text{C}-\text{D} \cdots \text{F}$ 3.946(38) Å) and forms considerable vdW potential overlap to aromatic rings ($\text{C} \cdots \text{C}$ 3.311(16) and 3.524(18) Å). The shorter $\text{C} \cdots \text{F}$ hydrogen bond and higher occupancy for site I indicate its higher binding energy. Notably, by forming new interactions,

the loading of the C_2D_2 molecule broke the original hydrogen bond inside the closed-pore UTSA-300a , accompanied by the inversion of distorted ligand conformation and subsequent rearrangement of interlayer stacking, which results in a fully expanded framework. This open-pore phase was then stabilized by C_2H_2 through strong host–guest interactions.

Based on the restored network structure, we can gain a further insight on the C_2H_2 adsorption mechanism in UTSA-300a . We conducted detailed first-principles dispersion-corrected density functional theory (DFT-D) calculations.²⁸ We found that the optimized C_2H_2 binding configurations are consistent with the experimental results from NPD data (Figure S25). The primary binding site locates at site I, at which dual $\text{C}-\text{H} \cdots \text{F}$ hydrogen bonding notably occurs between C_2H_2 and SiF_6^{2-} ($\text{H} \cdots \text{F}$ 1.832 Å, $\text{C}-\text{H} \cdots \text{F}$ 2.783 Å). The secondary binding site (at site II) exhibits a weak $\text{C}-\text{H} \cdots \text{F}$ hydrogen bonding ($\text{H} \cdots \text{F}$ 2.192 Å, $\text{C}-\text{H} \cdots \text{F}$ 3.134 Å). For the two binding sites, the DFT-D calculated static binding energy (E_B) is ~ 56.8 and ~ 51.7 kJ mol^{-1} , respectively. The binding affinity for C_2H_2 in UTSA-300a is comparable to the strongest calculated C_2H_2 binding strength in SIFSIX materials (~ 52.9 kJ mol^{-1} in SIFSIX-2-Cu-i).¹² Clearly, the electrostatic potential (negative) generated around SiF_6^{2-} induces the C_2H_2 molecule to primarily bind in a head-on orientation inside a pseudocubic cage, resulting the breaking of the original intranetwork hydrogen bonding and subsequent expansion to open-pore structure. In contrast, due to opposite molecular quadrupole moment (C_2H_2 , 20.5×10^{-40} C m^2 ; CO_2 , -13.4×10^{-40} C m^2),³¹ electrostatic repulsion between F sites and O atoms will form if CO_2 takes the same binding orientation (Figure 5). The

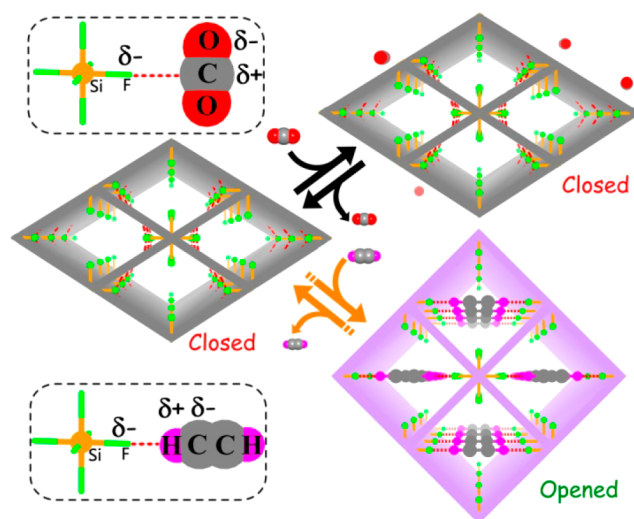


Figure 5. Schematic adsorption mechanism for CO_2 and C_2H_2 with different interactions under ambient conditions.

optimal sorption site for CO_2 is a different parallel orientation along metal hexafluorosilicate chains,³² which cannot break the original hydrogen bond under ambient conditions to open the closed-pore structure. The intranetwork hydrogen bonding is still relatively weak, so it can be broken under harsh conditions (lower temperatures and/or higher relative pressures), which has been commonly observed in flexible or dynamic MOFs.^{19a,33} Here, suitable pore size and geometry maximize the sieving effect of UTSA-300a . Moreover, benefiting from strong host–guest interactions between C_2H_2 (donor) and F sites (acceptor), the network structure can finally remain open.

These results from binding calculations are fully consistent with the high isosteric heats (Q_{st}) of C_2H_2 , as observed experimentally in **UTSA-300a**, and also explain well the unusual $\text{C}_2\text{H}_2/\text{CO}_2$ selectivity of **UTSA-300a**. Based on pure component isotherms at 273 and 298 K, the experimental adsorption enthalpy (Q_{st}) of C_2H_2 in **UTSA-300a** is evaluated by using the Clausius–Clapeyron equation (Figure 3c). The obtained Q_{st} value for C_2H_2 is 57.6 kJ mol^{-1} , obviously bigger than that in other SIFSIX materials (up to 41.9 kJ mol^{-1}).¹² This result indicates superior affinity of **UTSA-300a** toward C_2H_2 . Notably, smaller Q_{st} of about 30 kJ mol^{-1} was observed at high C_2H_2 loading, consistent with gradual expansion of network structure (energy consumed) during adsorption.

Next, to predict the potential of **UTSA-300a** in separation of the challenging $\text{C}_2\text{H}_2/\text{CO}_2$ and $\text{C}_2\text{H}_2/\text{C}_2\text{H}_4$ mixtures, the calculation was performed with the commonly used approach based on the ideal adsorbed solution theory (IAST, Figures S26–S33, Table S3). As expected, the simulated adsorption selectivities for the $\text{C}_2\text{H}_2/\text{CO}_2$ and $\text{C}_2\text{H}_2/\text{C}_2\text{H}_4$ binary equimolar mixtures are up to 743 and $>10^4$ at 298 K and 100 kPa, respectively, which is higher than those for any other MOF materials.^{12,19,29} Even higher selectivities of $>10^4$ were found at 273 K for both mixtures, as indicated by their isotherms. These highly pressure-dependent selectivities suggest that separation of these mixtures is feasible when it is performed under pressures above the gated opening pressure. The results fully support the potential in practical separation of $\text{C}_2\text{H}_2/\text{CO}_2$ and $\text{C}_2\text{H}_2/\text{C}_2\text{H}_4$ at ambient pressure.

To evaluate the $\text{C}_2\text{H}_2/\text{CO}_2$ and $\text{C}_2\text{H}_2/\text{C}_2\text{H}_4$ separation performances of **UTSA-300a** in practical adsorption processes, we carried out experimental breakthrough studies in which equimolar gas mixtures were flowed over a packed column of activated **UTSA-300a** solid with a total flow of 2 mL min^{-1} at 298 K (Figures S34 and S35). The results in Figure 6 (also

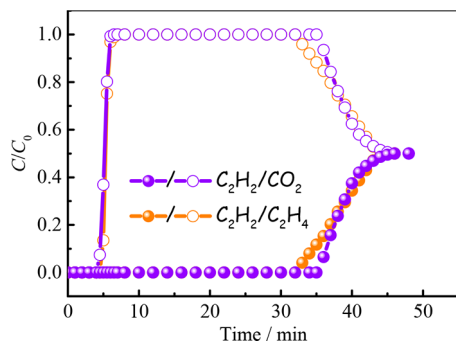


Figure 6. Experimental column breakthrough curves for equimolar $\text{C}_2\text{H}_2/\text{CO}_2$ (purple) and $\text{C}_2\text{H}_2/\text{C}_2\text{H}_4$ (orange) mixtures (298 K, 1 bar) in an adsorber bed packed with **UTSA-300a**. C_0 is the total concentration of gases at outlet.

Figure S36) indeed demonstrate that **UTSA-300a** is highly efficient for these challenging separations of $\text{C}_2\text{H}_2/\text{CO}_2$ and $\text{C}_2\text{H}_2/\text{C}_2\text{H}_4$ mixtures. For $\text{C}_2\text{H}_2/\text{CO}_2$ separation, gas chromatography data revealed that the outlet effluent gas during initial purges contains only CO_2 (purity $>99.9\%$), and this continues until C_2H_2 starts breaking through because its uptake capacity in **UTSA-300a** has been reached. Similar results can also be observed for the $\text{C}_2\text{H}_2/\text{C}_2\text{H}_4$ mixture, and the outlet C_2H_4 purity is also up to $>99.9\%$. For both gas mixtures, high-purity C_2H_2 ($>99\%$) can be obtained during the final regeneration stage. Notably, the breakthrough curves for both gas mixtures

are almost the same (elution times $>30 \text{ min}$), suggesting the same C_2H_2 capture capacities for **UTSA-300a** to these mixtures, which demonstrates that the molecular exclusion of CO_2 and C_2H_4 works well even under dynamic gas mixture flow. Further studies for **UTSA-300a** with larger gas flow (see Figures S37 and S38) also show excellent separation performance toward challenging $\text{C}_2\text{H}_2/\text{CO}_2$ and $\text{C}_2\text{H}_2/\text{C}_2\text{H}_4$ mixtures.

CONCLUSION

In summary, we have realized a novel porous metal–organic framework **UTSA-300** toward recognition of a specific gas molecule from its very similar impurity. In principle, fine-tuning of pore size in MOFs can gain a sieving effect for gas separation, which is particularly effective for molecules with different sizes and shapes. To further separate much more challenging molecules with very similar sizes and physical properties, we unexpectedly reveal a unique approach to utilize a size-matched pore with strong binding sites and dynamic pore structures to bind targeted molecules for the highly selective gas separation. The size match and orientation binding mode have enlarged the tiny difference between C_2H_2 and CO_2 , leading to their diametrically different adsorption capacities. The recognition mechanism for gas molecules is well supported by direct crystallography studies in which the anisotropic adsorption site within the framework only allows C_2H_2 to open the pore structure by forming strong host–guest interactions. This approach is likely applicable to other gas mixtures, which will facilitate the design and implementation of novel porous MOF materials for other important gas separations.

ASSOCIATED CONTENT

Supporting Information

The Supporting Information is available free of charge on the ACS Publications website at DOI: 10.1021/jacs.7b03850.

Crystallographic data, additional structural plot, TG curves, PXRD, multiple cycle sorption isotherm, NPD data for Rietveld refinement, results of density functional theory calculations, dual Langmuir–Freundlich isotherm model fitting, isosteric heat of adsorption calculation, IAST calculations of adsorption selectivities, and column breakthrough test setup with procedures and measurements (PDF)

Crystallographic data for **UTSA-300** $\cdot\text{H}_2\text{O}$ (CIF)

Crystallographic data for **UTSA-300a** (CIF)

Crystallographic data for **UTSA-300** $\cdot\text{C}_2\text{D}_2$ (CIF)

AUTHOR INFORMATION

Corresponding Authors

*wzhou@nist.gov

*banglin.chen@utsa.edu

ORCID

Rui-Biao Lin: 0000-0003-3267-220X

Hui Wu: 0000-0003-0296-5204

Bin Li: 0000-0002-7774-5452

Wei Zhou: 0000-0002-5461-3617

Banglin Chen: 0000-0001-8707-8115

Notes

The authors declare no competing financial interest.

■ ACKNOWLEDGMENTS

This work was supported by Grant AX-1730 from the Welch Foundation (B.C.).

■ REFERENCES

- (1) Pässler, P.; Hefner, W.; Buckl, K.; Meinass, H.; Meiswinkel, A.; Wernicke, H.-J.; Ebersberg, G.; Müller, R.; Bässler, J.; Behringer, H.; Mayer, D. *Ullmann's Encyclopedia of Industrial Chemistry*; Wiley-VCH: Weinheim, Germany, 2000.
- (2) Reid, C. R.; Thomas, K. M. *J. Phys. Chem. B* **2001**, *105*, 10619.
- (3) (a) Furukawa, H.; Cordova, K. E.; O'Keeffe, M.; Yaghi, O. M. *Science* **2013**, *341*, 1230444. (b) Kitagawa, S.; Kitaura, R.; Noro, S.-i. *Angew. Chem., Int. Ed.* **2004**, *43*, 2334. (c) Li, B.; Wen, H.-M.; Cui, Y.; Zhou, W.; Qian, G.; Chen, B. *Adv. Mater.* **2016**, *28*, 8819. (d) Wang, C.; Liu, D.; Lin, W. *J. Am. Chem. Soc.* **2013**, *135*, 13222. (e) Cui, Y.; Li, B.; He, H.; Zhou, W.; Chen, B.; Qian, G. *Acc. Chem. Res.* **2016**, *49*, 483.
- (4) (a) Moreau, F.; da Silva, I.; Al Smail, N. H.; Easun, T. L.; Savage, M.; Godfrey, H. G. W.; Parker, S. F.; Manuel, P.; Yang, S.; Schröder, M. *Nat. Commun.* **2017**, *8*, 14085. (b) Taylor, M. K.; Runčevski, T.; Oktawiec, J.; Gonzalez, M. I.; Siegelman, R. L.; Mason, J. A.; Ye, J.; Brown, C. M.; Long, J. R. *J. Am. Chem. Soc.* **2016**, *138*, 15019.
- (5) (a) Qiu, S.; Xue, M.; Zhu, G. *Chem. Soc. Rev.* **2014**, *43*, 6116. (b) Gelfand, B. S.; Huynh, R. P. S.; Mah, R. K.; Shimizu, G. K. H. *Angew. Chem., Int. Ed.* **2016**, *55*, 14614.
- (6) (a) Hu, Z.; Deibert, B. J.; Li, J. *Chem. Soc. Rev.* **2014**, *43*, 5815. (b) Lin, R.-B.; Li, F.; Liu, S.-Y.; Qi, X.-L.; Zhang, J.-P.; Chen, X.-M. *Angew. Chem., Int. Ed.* **2013**, *52*, 13429.
- (7) (a) Zhu, Q.-L.; Li, J.; Xu, Q. *J. Am. Chem. Soc.* **2013**, *135*, 10210. (b) Li, B.; Leng, K.; Zhang, Y.; Dynes, J. J.; Wang, J.; Hu, Y.; Ma, D.; Shi, Z.; Zhu, L.; Zhang, D.; Sun, Y.; Chrzanowski, M.; Ma, S. *J. Am. Chem. Soc.* **2015**, *137*, 4243. (c) Noh, H.; Cui, Y.; Peters, A. W.; Pahls, D. R.; Ortuño, M. A.; Vermeulen, N. A.; Cramer, C. J.; Gagliardi, L.; Hupp, J. T.; Farha, O. K. *J. Am. Chem. Soc.* **2016**, *138*, 14720.
- (8) Zhao, X.; Mao, C.; Luong, K. T.; Lin, Q.; Zhai, Q.-G.; Feng, P.; Bu, X. *Angew. Chem., Int. Ed.* **2016**, *55*, 2768.
- (9) (a) Xu, R.; Wang, Y.; Duan, X.; Lu, K.; Micheroni, D.; Hu, A.; Lin, W. *J. Am. Chem. Soc.* **2016**, *138*, 2158. (b) Horcajada, P.; Gref, R.; Baati, T.; Allan, P. K.; Maurin, G.; Couvreur, P.; Férey, G.; Morris, R. E.; Serre, C. *Chem. Rev.* **2012**, *112*, 1232.
- (10) (a) Zhou, H.-C.; Kitagawa, S. *Chem. Soc. Rev.* **2014**, *43*, 5415. (b) Zhou, H.-C.; Long, J. R.; Yaghi, O. M. *Chem. Rev.* **2012**, *112*, 673.
- (11) (a) Zhang, Y.-B.; Furukawa, H.; Ko, N.; Nie, W.; Park, H. J.; Okajima, S.; Cordova, K. E.; Deng, H.; Kim, J.; Yaghi, O. M. *J. Am. Chem. Soc.* **2015**, *137*, 2641. (b) Zhai, Q.-G.; Bu, X.; Mao, C.; Zhao, X.; Daemen, L.; Cheng, Y.; Ramirez-Cuesta, A. J.; Feng, P. *Nat. Commun.* **2016**, *7*, 13645. (c) Yuan, S.; Chen, Y.-P.; Qin, J.-S.; Lu, W.; Zou, L.; Zhang, Q.; Wang, X.; Sun, X.; Zhou, H.-C. *J. Am. Chem. Soc.* **2016**, *138*, 8912. (d) Krause, S.; Bon, V.; Senkovska, I.; Stoeck, U.; Wallacher, D.; Többs, D. M.; Zander, R. S.; Maurin, G.; Coudert, F. o.-X.; Kaskel, S. *Nature* **2016**, *532*, 348. (e) Bao, Z.; Chang, G.; Xing, H.; Krishna, R.; Ren, Q.; Chen, B. *Energy Environ. Sci.* **2016**, *9*, 3612. (f) He, Y.; Krishna, R.; Chen, B. *Energy Environ. Sci.* **2012**, *5*, 9107. (g) Xiang, S.; He, Y.; Zhang, Z.; Wu, H.; Zhou, W.; Krishna, R.; Chen, B. *Nat. Commun.* **2012**, *3*, 954.
- (12) Cui, X.; Chen, K.; Xing, H.; Yang, Q.; Krishna, R.; Bao, Z.; Wu, H.; Zhou, W.; Dong, X.; Han, Y.; Li, B.; Ren, Q.; Zaworotko, M. J.; Chen, B. *Science* **2016**, *353*, 141.
- (13) Liu, C.; Zeng, C.; Luo, T.-Y.; Merg, A. D.; Jin, R.; Rosi, N. L. *J. Am. Chem. Soc.* **2016**, *138*, 12045.
- (14) Chen, K.-J.; Madden, D. G.; Pham, T.; Forrest, K. A.; Kumar, A.; Yang, Q.-Y.; Xue, W.; Space, B.; Perry, J. J.; Zhang, J.-P.; Chen, X.-M.; Zaworotko, M. J. *Angew. Chem., Int. Ed.* **2016**, *55*, 10268.
- (15) Assen, A. H.; Belmabkhout, Y.; Adil, K.; Bhatt, P. M.; Xue, D.-X.; Jiang, H.; Eddaoudi, M. *Angew. Chem., Int. Ed.* **2015**, *54*, 14353.
- (16) Cadiau, A.; Adil, K.; Bhatt, P. M.; Belmabkhout, Y.; Eddaoudi, M. *Science* **2016**, *353*, 137.
- (17) Luo, F.; Yan, C.; Dang, L.; Krishna, R.; Zhou, W.; Wu, H.; Dong, X.; Han, Y.; Hu, T.-L.; O'Keeffe, M.; Wang, L.; Luo, M.; Lin, R.-B.; Chen, B. *J. Am. Chem. Soc.* **2016**, *138*, 5678.
- (18) Chen, K.-J.; Scott, H. S.; Madden, D. G.; Pham, T.; Kumar, A.; Bajpai, A.; Lusi, M.; Forrest, K. A.; Space, B.; Perry, J. J., IV; Zaworotko, M. J. *Chem.* **2016**, *1*, 753.
- (19) (a) Foo, M. L.; Matsuda, R.; Hijikata, Y.; Krishna, R.; Sato, H.; Horike, S.; Hori, A.; Duan, J.; Sato, Y.; Kubota, Y.; Takata, M.; Kitagawa, S. *J. Am. Chem. Soc.* **2016**, *138*, 3022. (b) Zhang, J.-P.; Chen, X.-M. *J. Am. Chem. Soc.* **2009**, *131*, 5516.
- (20) *Crystal Clear*; Rigaku/MSO, Inc., Rigaku Corporation: The Woodlands, TX, 2005.
- (21) Higashi, T. *ABSCOR*; Rigaku Corporation: Tokyo, Japan, 1995.
- (22) Sheldrick, G. *Acta Crystallogr., Sect. A: Found. Crystallogr.* **2008**, *64*, 112.
- (23) Larson, A. C.; Von Dreele, R. B. *General Structure Analysis System, Report LAUR 86-748*; Los Alamos National Laboratory: Los Alamos, NM, 1994.
- (24) Giannozzi, P.; Baroni, S.; Bonini, N.; Calandra, M.; Car, R.; Cavazzoni, C.; Ceresoli, D.; Chiarotti, G. L.; Cococcioni, M.; Dabo, I.; Dal Corso, A.; de Gironcoli, S.; Fabris, S.; Fratesi, G.; Gebauer, R.; Gerstmann, U.; Gougousis, C.; Kokalj, A.; Lazzeri, M.; Martin-Samos, L.; Marzari, N.; Mauri, F.; Mazzarello, R.; Paolini, S.; Pasquarello, A.; Paulatto, L.; Sbraccia, C.; Scandolo, S.; Sclauzero, G.; Seitsonen, A. P.; Smogunov, A.; Umari, P.; Wentzcovitch, R. M. *J. Phys.: Condens. Matter* **2009**, *21*, 395502.
- (25) Barone, V.; Casarin, M.; Forrer, D.; Pavone, M.; Sami, M.; Vittadini, A. *J. Comput. Chem.* **2009**, *30*, 934.
- (26) Nugent, P.; Belmabkhout, Y.; Burd, S. D.; Cairns, A. J.; Luebke, R.; Forrest, K.; Pham, T.; Ma, S.; Space, B.; Wojtas, L.; Eddaoudi, M.; Zaworotko, M. J. *Nature* **2013**, *495*, 80.
- (27) Uemura, K.; Maeda, A.; Maji, T. K.; Kanoo, P.; Kita, H. *Eur. J. Inorg. Chem.* **2009**, *2009*, 2329.
- (28) Hu, T.-L.; Wang, H.; Li, B.; Krishna, R.; Wu, H.; Zhou, W.; Zhao, Y.; Han, Y.; Wang, X.; Zhu, W.; Yao, Z.; Xiang, S.; Chen, B. *Nat. Commun.* **2015**, *6*, 7328.
- (29) Hazra, A.; Jana, S.; Bonakala, S.; Balasubramanian, S.; Maji, T. K. *Chem. Commun.* **2017**, *53*, 4907.
- (30) Li, L.; Krishna, R.; Wang, Y.; Wang, X.; Yang, J.; Li, J. *Eur. J. Inorg. Chem.* **2016**, *2016*, 4457.
- (31) Junquera-Hernández, J. M.; Sánchez-Marín, J.; Maynau, D. *Chem. Phys. Lett.* **2002**, *359*, 343.
- (32) Ziaee, A.; Chovan, D.; Lusi, M.; Perry, J. J.; Zaworotko, M. J.; Tofail, S. A. M. *Cryst. Growth Des.* **2016**, *16*, 3890.
- (33) Mason, J. A.; Oktawiec, J.; Taylor, M. K.; Hudson, M. R.; Rodriguez, J.; Bachman, J. E.; Gonzalez, M. I.; Cervellino, A.; Guagliardi, A.; Brown, C. M.; Llewellyn, P. L.; Masciocchi, N.; Long, J. R. *Nature* **2015**, *527*, 357.

Supporting Information

Optimized Separation of Acetylene from Carbon Dioxide and Ethylene in a Microporous Material

Rui-Biao Lin,¹ Libo Li,^{1,3} Hui Wu,² Hadi Arman,¹ Bin Li,¹ Rong-Guang Lin,^{1,4} Wei

*Zhou,^{*2} Banglin Chen^{*1}*

¹Department of Chemistry, University of Texas at San Antonio One UTSA Circle,
San Antonio, Texas 78249-0698, USA Fax: (+1)210-458-7428, E-mail:
banglin.chen@utsa.edu

²NIST Center for Neutron Research, National Institute of Standards and Technology,
Gaithersburg, Maryland 20899-6102, USA, E-mail: wzhou@nist.gov

³Research Institute of Special Chemicals, Taiyuan University of Technology, Taiyuan
030024, Shanxi, China.

⁴School of Life Sciences, Fujian Agriculture and Forestry University, Fuzhou 350002,
China

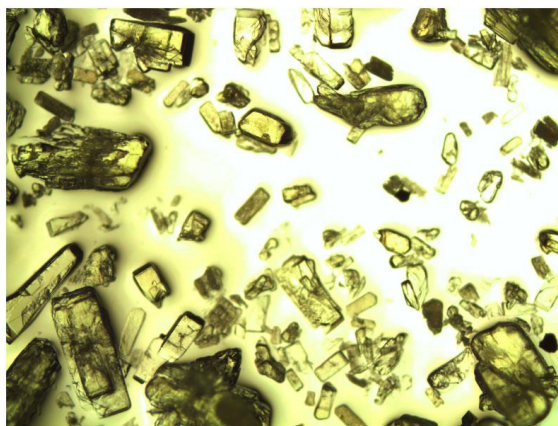


Figure S1. Optical image of as-synthesized UTSA-300.

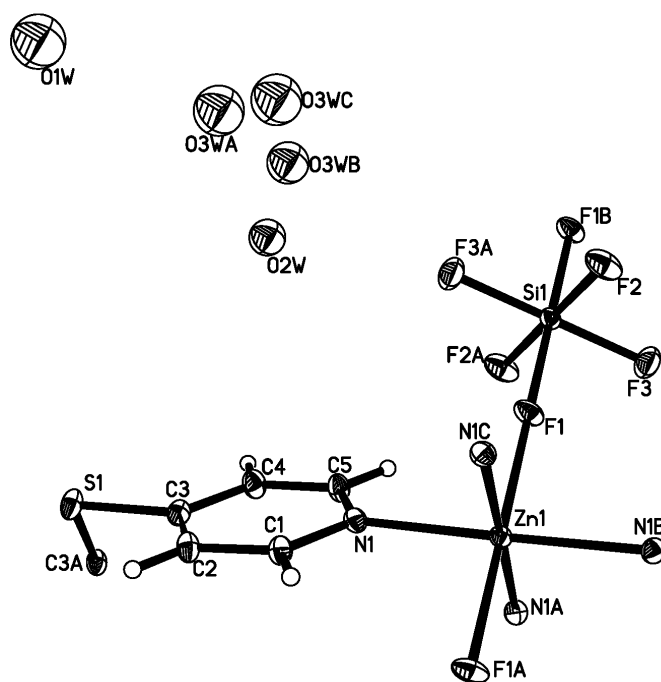


Figure S2. The coordination environments in as-synthesized UTSA-300 (see details in supplementary crystallographic data and Table S1).

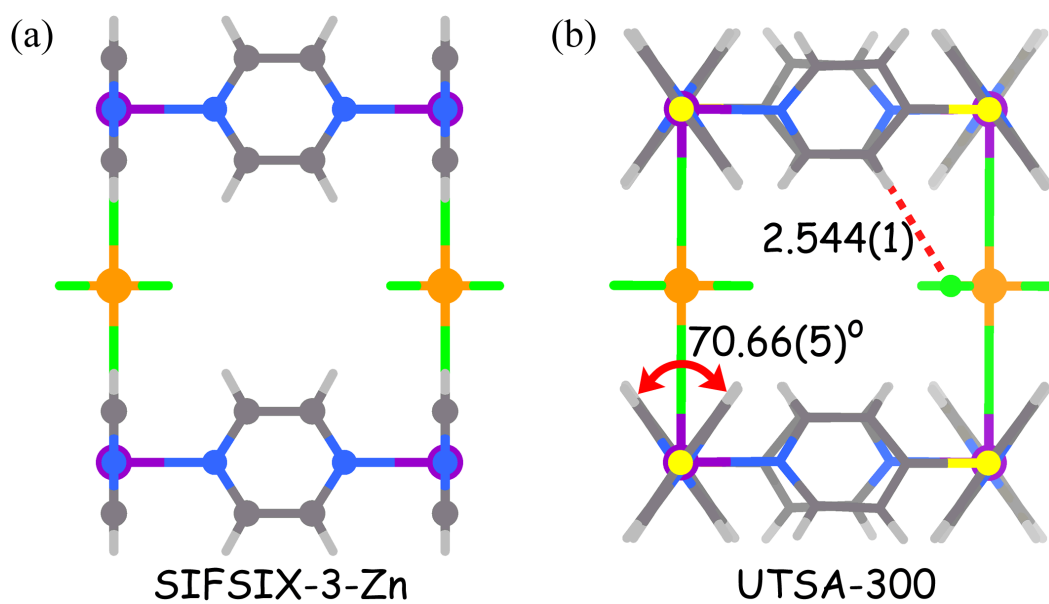


Figure S3. Comparison of the cage units between SIFSIX-3-Zn (a) and as-synthesized UTSA-300 (b).

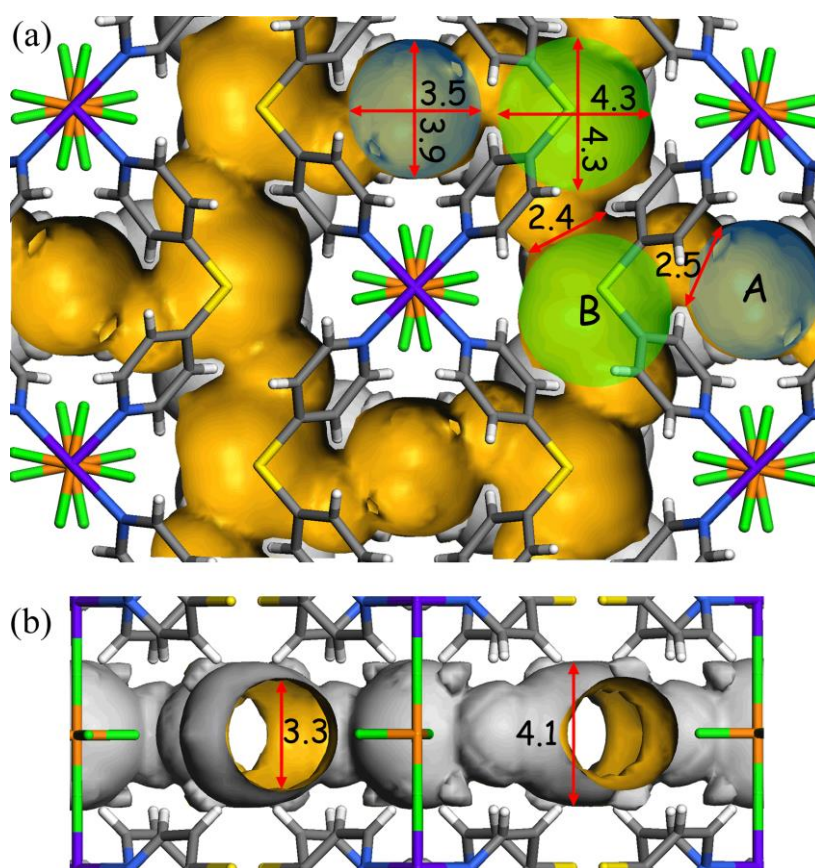


Figure S4. Pore geometry and dimensions of as-synthesized UTSA-300.

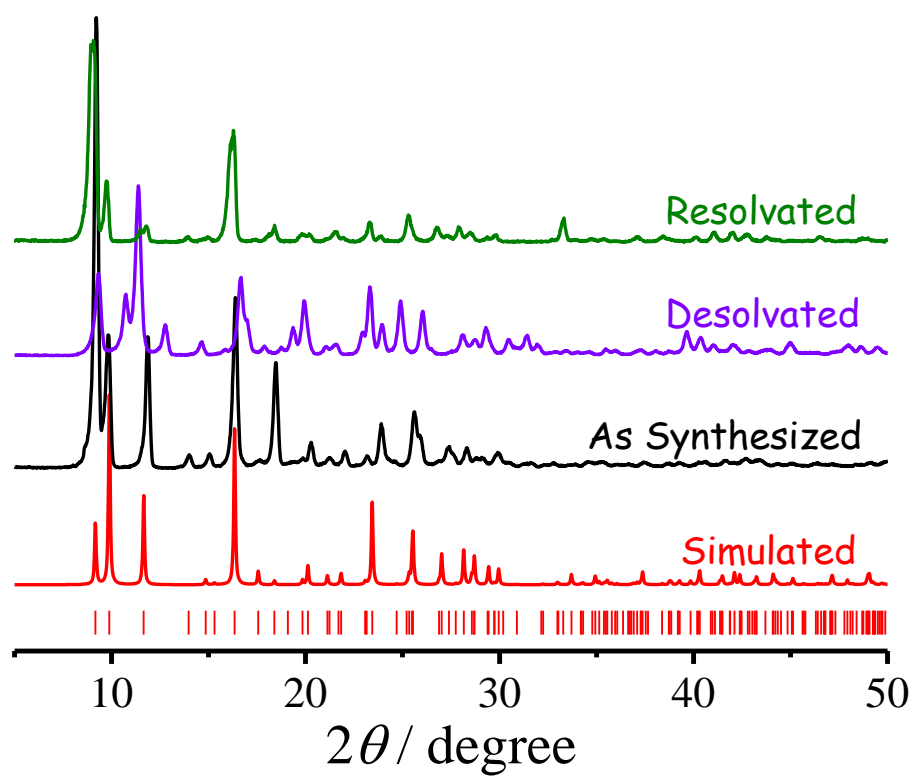


Figure S5. PXRD patterns of **UTSA-300**.

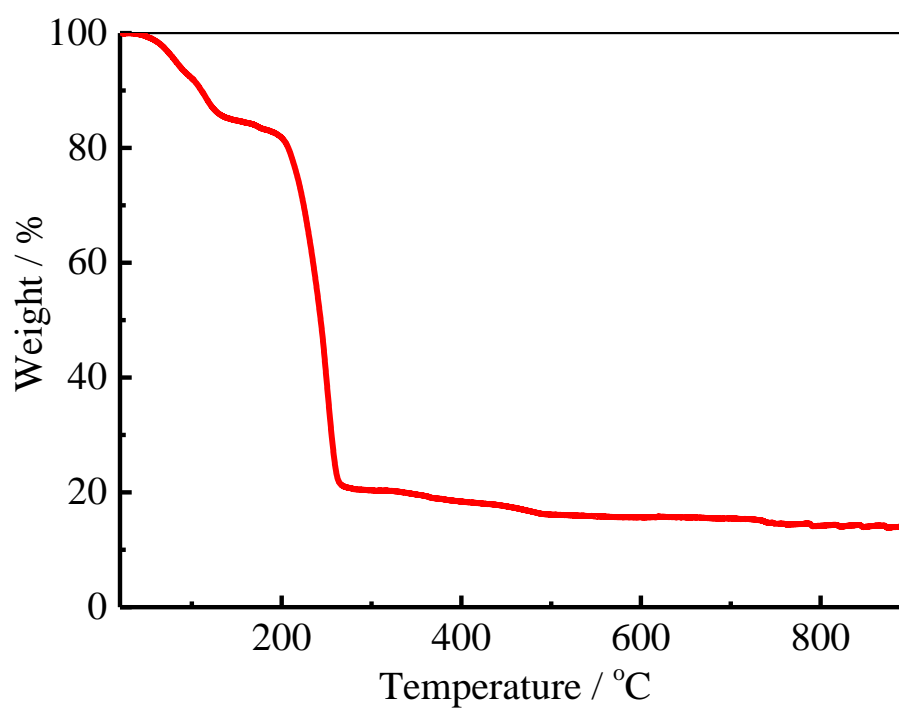


Figure S6. TGA curve of **UTSA-300-H₂O**.

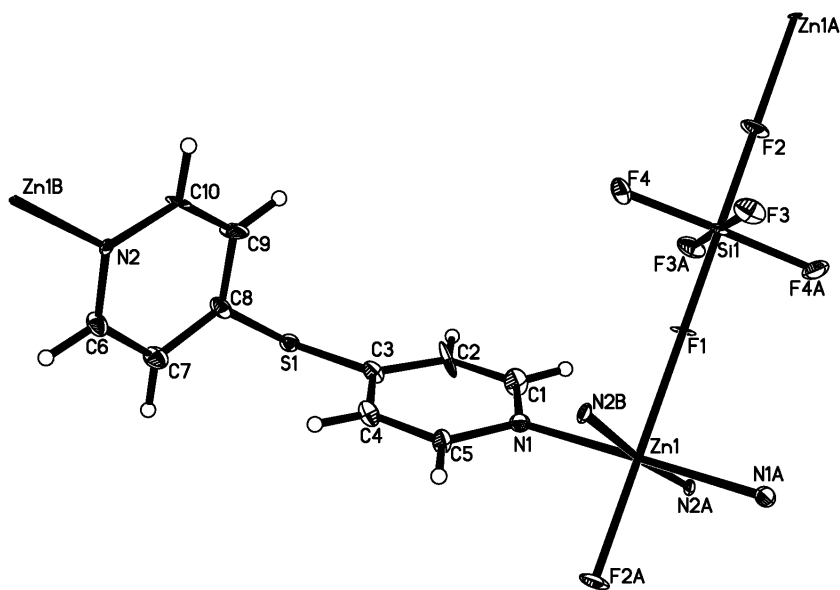


Figure S7. Single crystal X-ray diffraction data of activated **UTSA-300a**. Crystal data: $C_{20}H_{16}F_6N_4S_2SiZn$, monoclinic, space group $P2_1/n$ (No. 13), $a = 10.1298(10)$, $b = 7.5694(9)$, $c = 16.625(2)$ Å, $\beta = 103.041(12)^\circ$, $V = 1241.9(3)$ Å³, $Z = 2$, $T = 150$ K. 14671 reflections measured, 6904 unique ($R_{int} = 0.1989$) used in all calculations. The final agreement index R_1 was 0.2656 for 3842 independent significant [$I > 2\sigma(I)$] absorption corrected data and 156 parameters, [$wR_2 = 0.5937$ for all data], GOF = 1.724. Highest peak of residual electron density is 6.57 eÅ^{-3} (0.66 Å from Zn1) and deepest hole is -8.024 eÅ^{-3} (1.29 Å from C5).

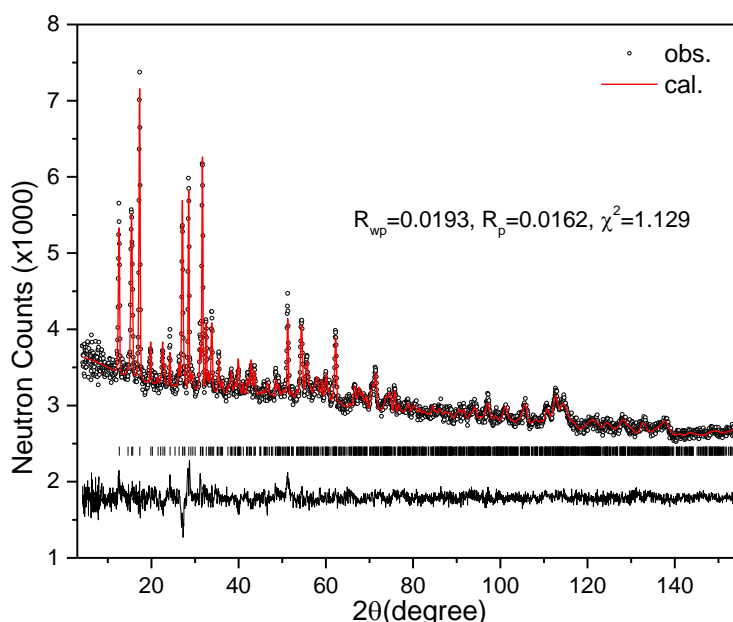


Figure S8. Experimental (circles), calculated (line), and difference (line below observed and calculated patterns) neutron powder diffraction profiles for **UTSA-300a**, measured at 296 K. The ligand molecules were kept as rigid bodies during the Rietveld structural refinement. Vertical bars indicate the calculated positions of Bragg peaks. Goodness of fit data are shown in insets.

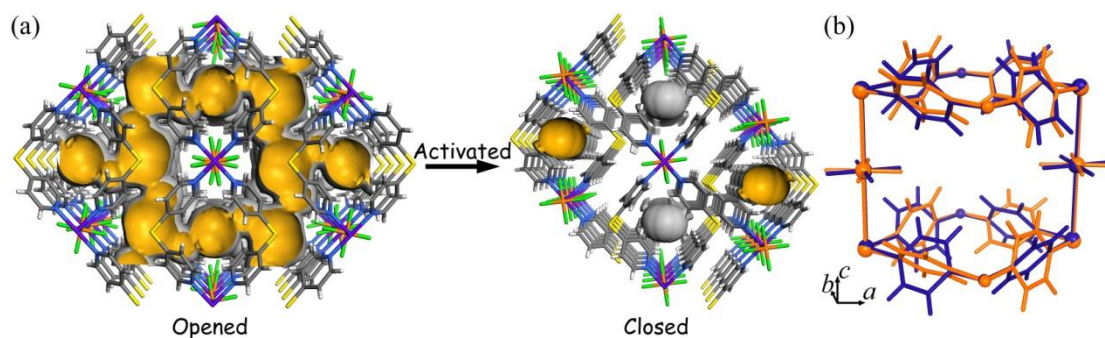


Figure S9. (a) Porosity change during transformation from as-synthesized **UTSA-300** to desolvated one, and (b) their corresponding cage units (indigo and orange, respectively).

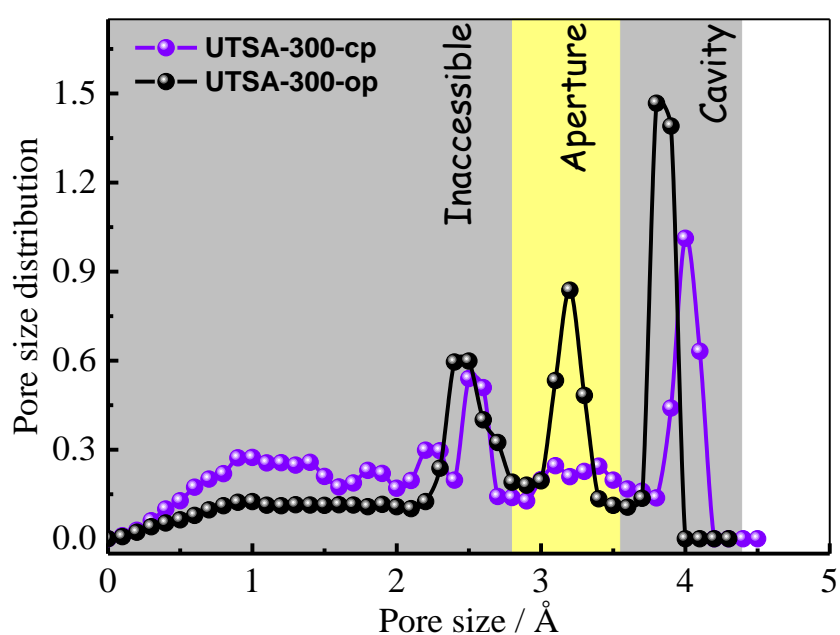


Figure S10. Pore size distribution (PSD) of close and open phases of **UTSA-300**. PSD was calculated using the well-known method by Gubbins et al.^{S1} The van der Waals diameters of the framework atoms were adopted from the Cambridge Crystallographic Center.

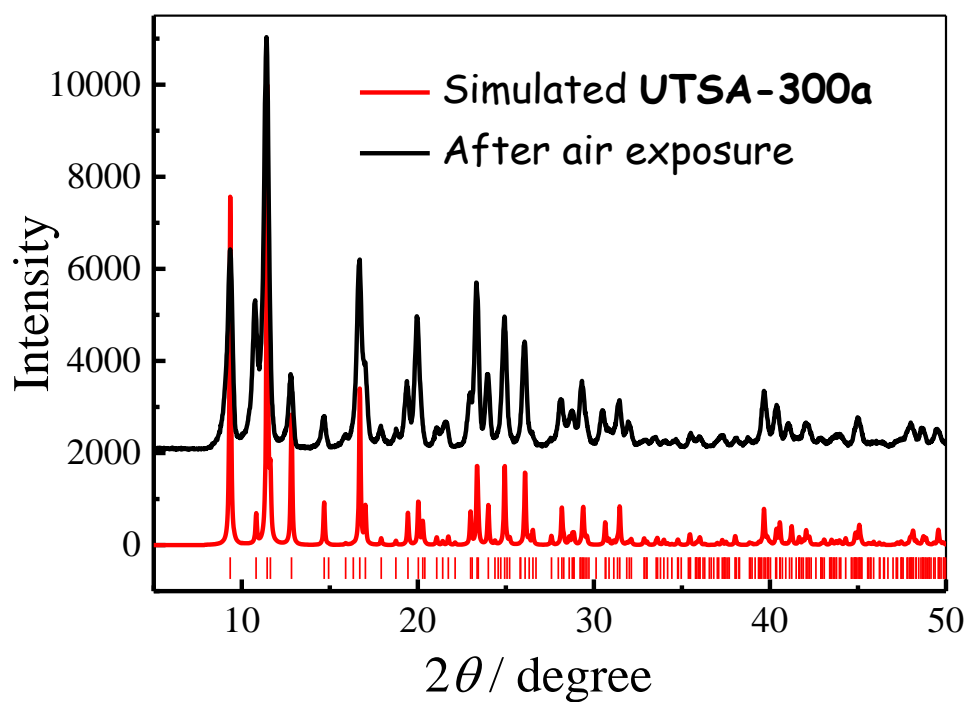


Figure S11. PXRD patterns of **UTSA-300a**.

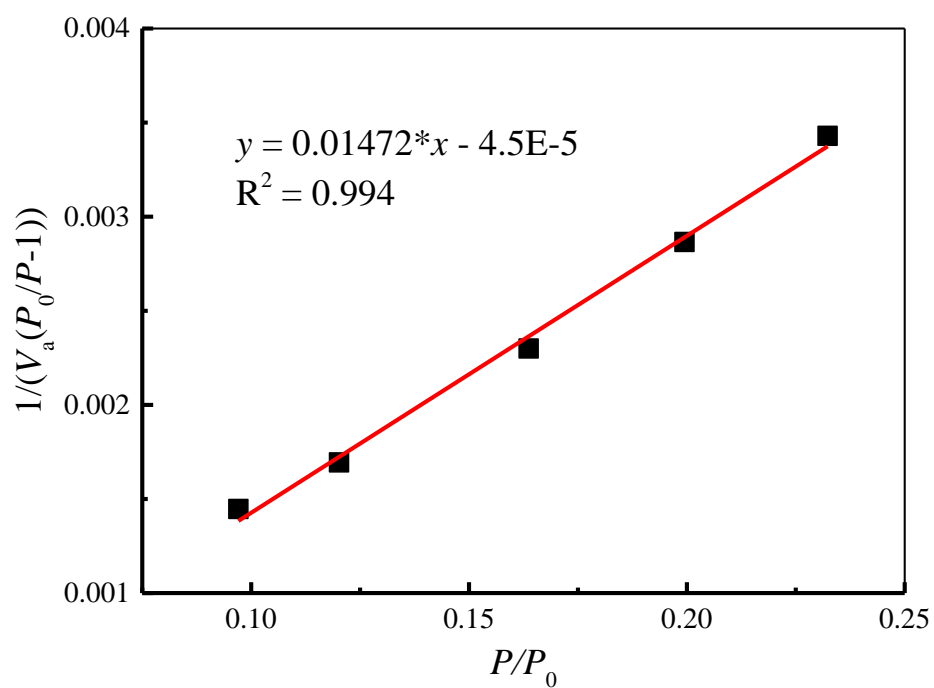


Figure S12. BET calculation based on CO₂ adsorption isotherm of **UTSA-300a** at 195 K.

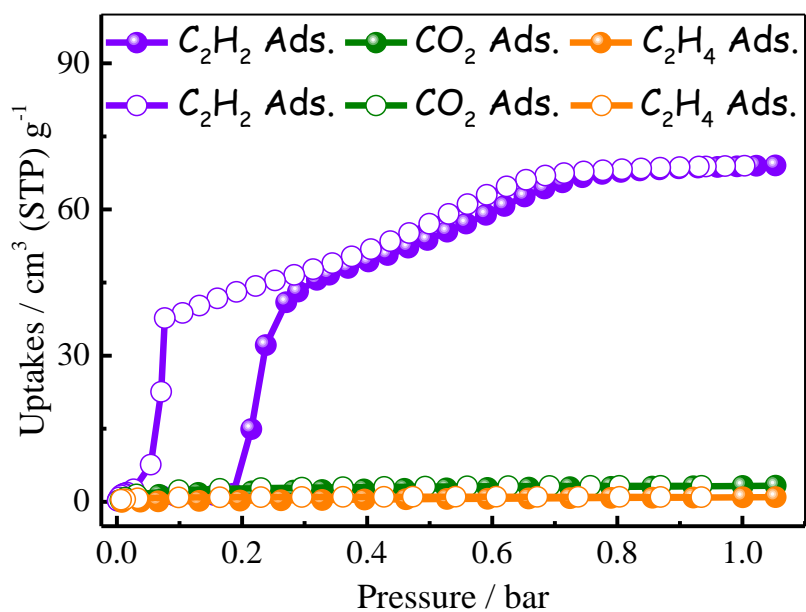


Figure S13. C_2H_2 , CO_2 and C_2H_4 sorption isotherms for **UTSA-300a** at 298 K.

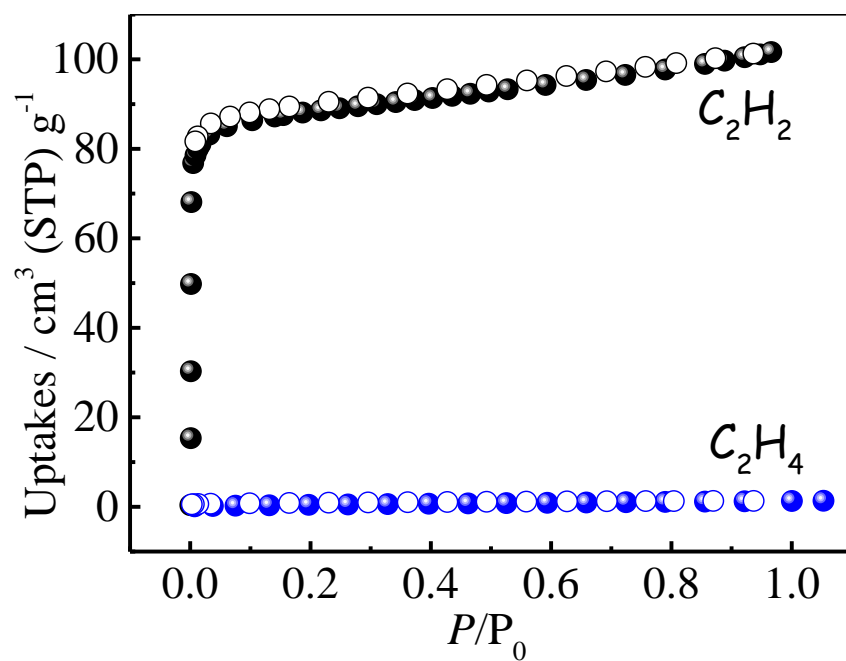


Figure S14. C_2H_2 and C_2H_4 sorption isotherms for **UTSA-300a** at 195 K.

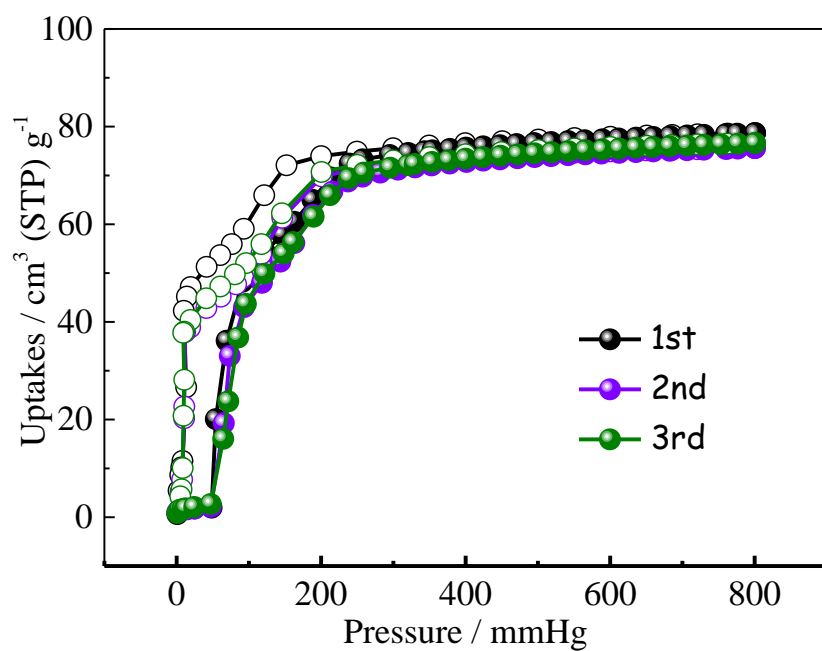


Figure S15. Multiple cycles of C_2H_2 sorption measurements for **UTSA-300a** at 273 K.

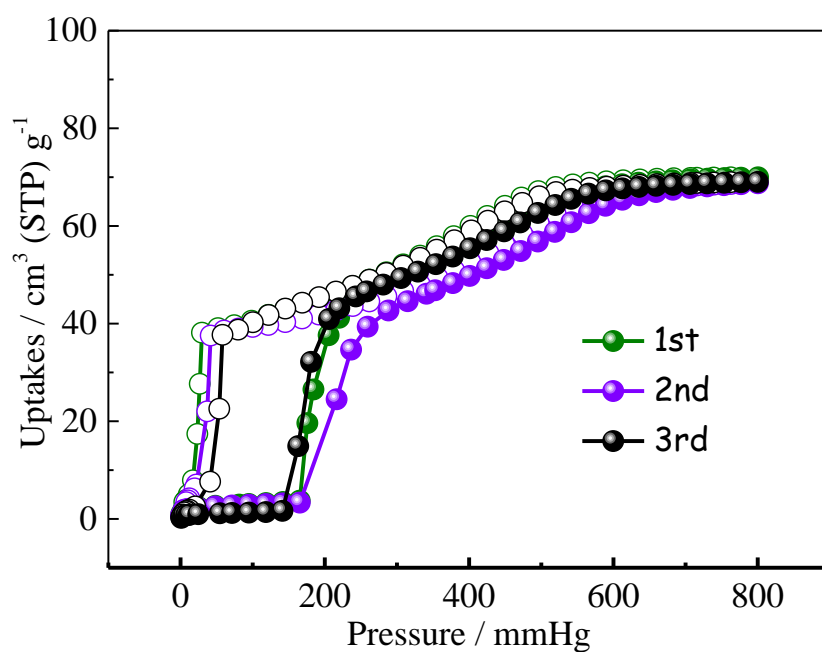


Figure S16. Multiple cycles of C_2H_2 sorption measurements for **UTSA-300a** at 298 K.

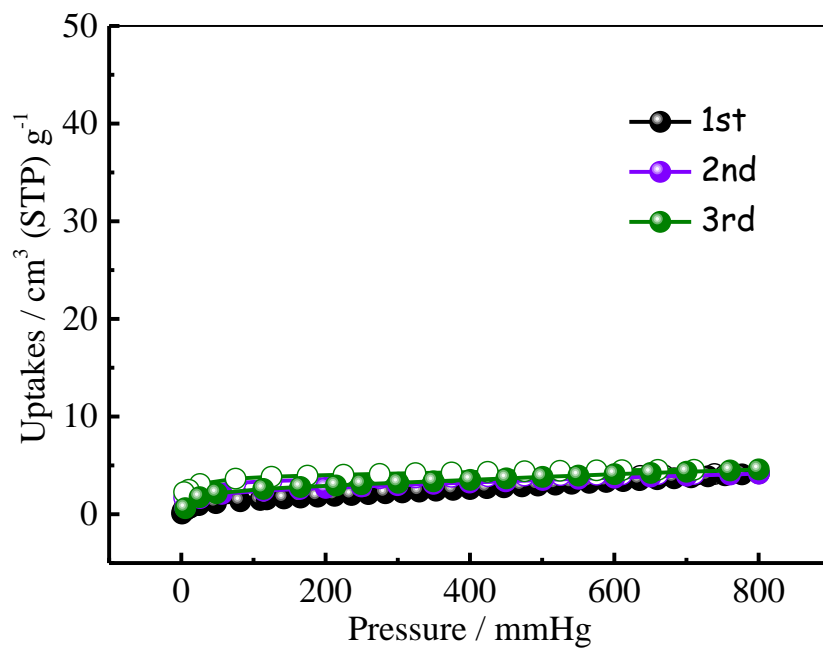


Figure S17. Multiple cycles of CO₂ sorption measurements for **UTSA-300a** at 273 K.

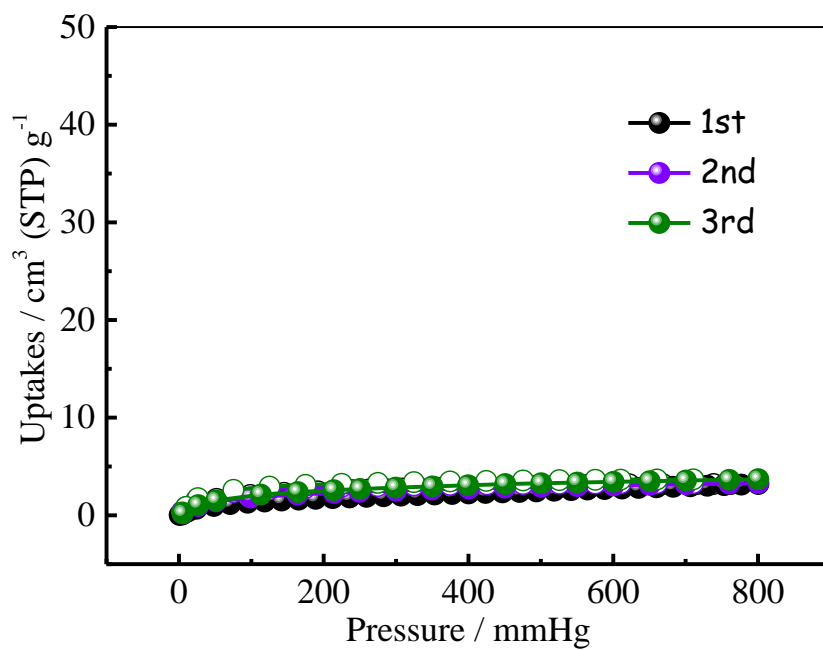


Figure S18. Multiple cycles of CO₂ sorption measurements for **UTSA-300a** at 298 K.

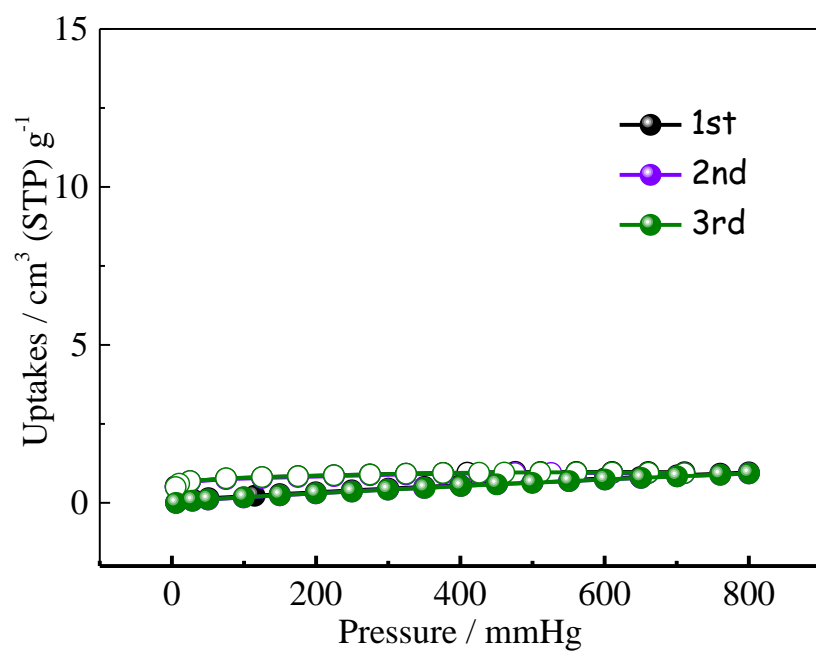


Figure S19. Multiple cycles of C_2H_4 sorption measurements for **UTSA-300a** at 273 K.

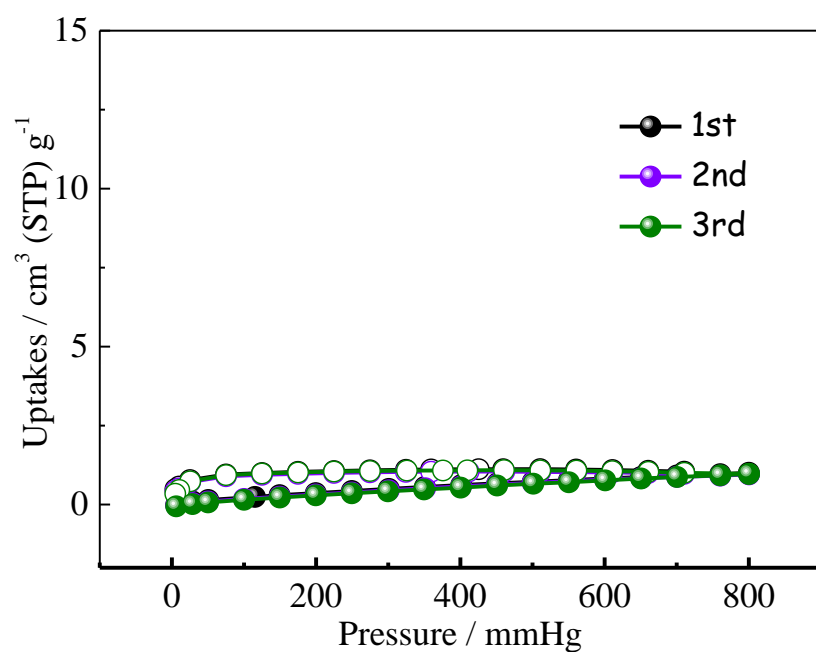


Figure S20. Multiple cycles of C_2H_4 sorption measurements for **UTSA-300a** at 298 K.

Neutron diffraction

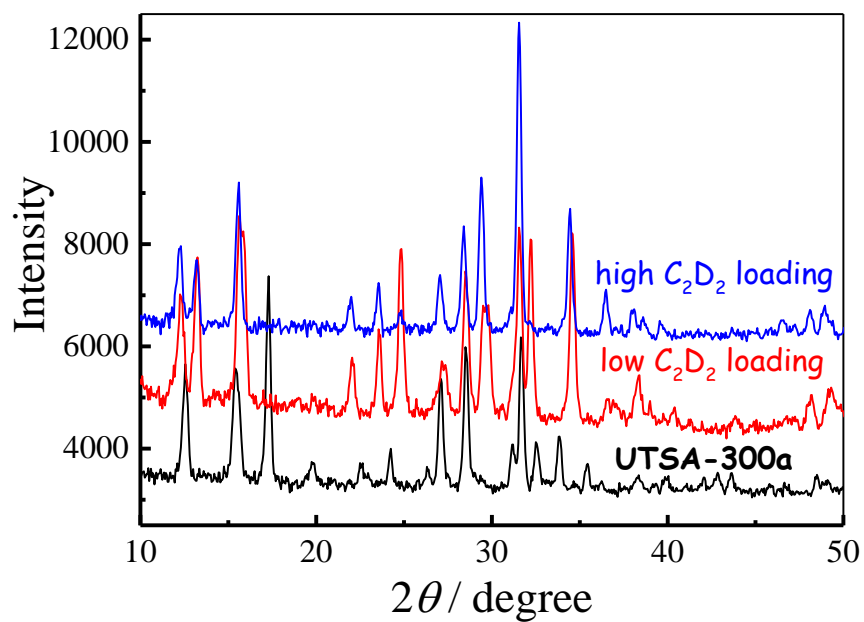


Figure S21. Measured neutron powder diffraction data for **UTSA-300a** loaded with C_2D_2 .

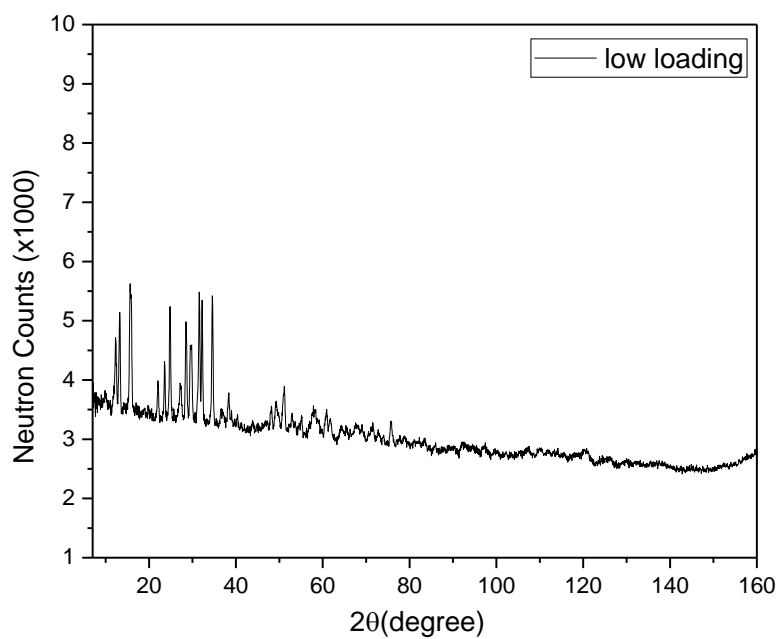


Figure S22. Neutron powder diffraction data for **UTSA-300a** loaded with C_2D_2 (equilibrated at 296 K and 0.35 bar) measured at 296 K.

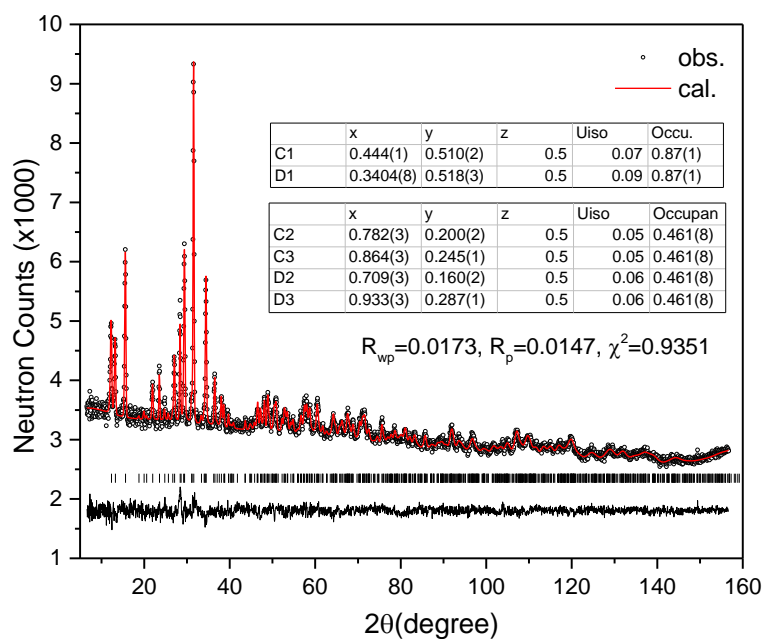


Figure S23. Rietveld refinements of the neutron powder diffraction data for **UTSA-300a** loaded with C_2D_2 (equilibrated at 296 K and 0.8 bar) measured at 296 K. The ligand molecules and the C_2D_2 molecules were kept as rigid bodies during the refinement. Experimental (circles), calculated (line), and difference (line below observed and calculated patterns) neutron powder diffraction profiles are shown. Vertical bars indicate the calculated positions of Bragg peaks. Goodness of fit data are shown in insets.

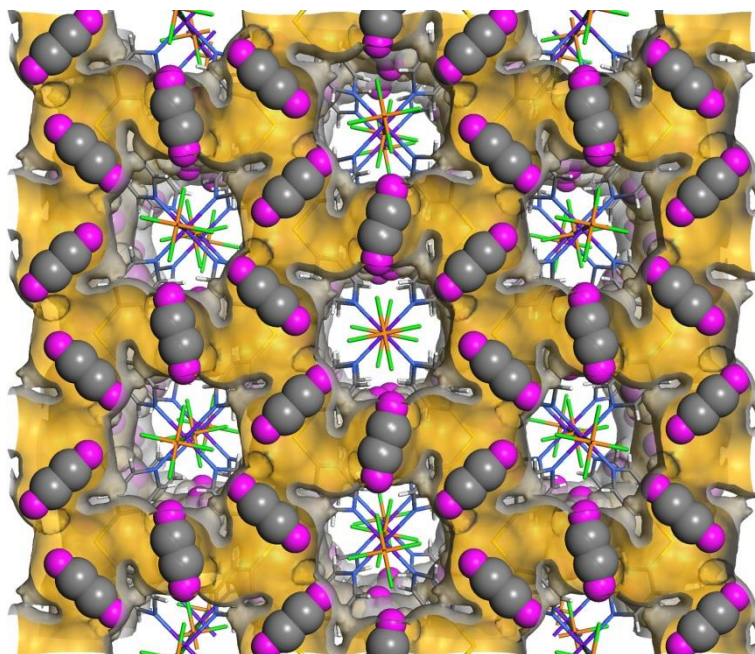


Figure S24. Packing diagram of **UTSA-300** \supset C_2D_2 .

Density-functional theory calculations

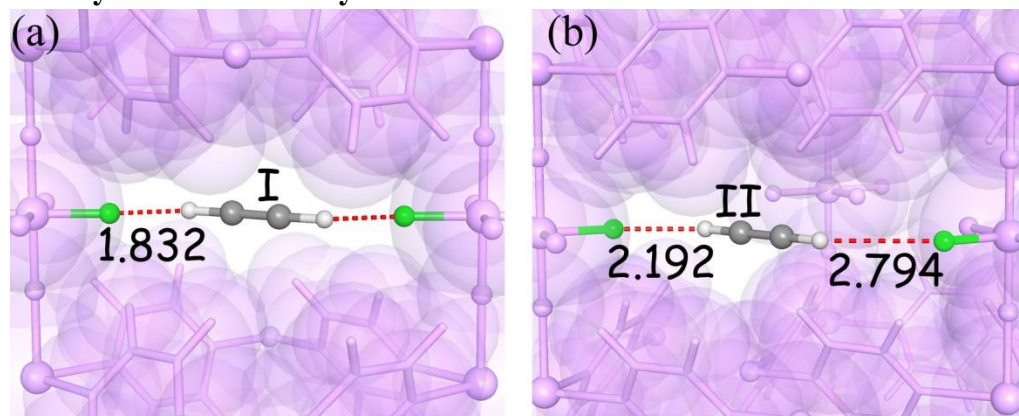


Figure S25. DFT-D optimized C_2H_2 adsorption sites of **UTSA-300a**.

Calculation of isosteric heat of adsorption (Q_{st}).

The Clausius-Clapeyron equation was employed to calculate the enthalpies of C_2H_2 adsorption:

$$\frac{\partial(\ln P)}{\partial(1/T)} = -\frac{Q_{st}}{R}$$

Where P is the pressure, T is the temperature, R is the universal gas constant.

IAST Calculation. In order to calculate the selective sorption performance of **UTSA-300a** toward the separation of binary mixed gases, the fitting of the single-component C_2H_2 , CO_2 , and C_2H_4 adsorption isotherms was carried out based on the dual-site Langmuir-Freundlich (DSLFF) model. The fitting parameters of the DSLF equation are displayed in Table S3. Adsorption isotherms and gas selectivities of mixed C_2H_2/CO_2 (50/50, v/v) and C_2H_2/C_2H_4 (50/50, v/v) at 273 and 296 K for **UTSA-300a** were predicted using the ideal adsorbed solution theory (IAST). The results are shown in Fig. S26-27.

Dual-site Langmuir-Freundlich (DSLFF) model is listed as below:

$$N = N_1^{\max} \times \frac{b_1 p^{1/n_1}}{1 + b_1 p^{1/n_1}} + N_2^{\max} \times \frac{b_2 p^{1/n_2}}{1 + b_2 p^{1/n_2}}$$

Where p (unit: kPa) is the pressure of the bulk gas at equilibrium with the adsorbed phase, N (unit: mol/kg) is the adsorbed amount per mass of adsorbent, N_1^{\max} and N_2^{\max} (unit: mmol/g) are the saturation capacities of two different sites, b_1 and b_2 (unit: 1/kPa) are the affinity coefficients of these sites, and n_1 and n_2 represent the deviations from an ideal homogeneous surface.

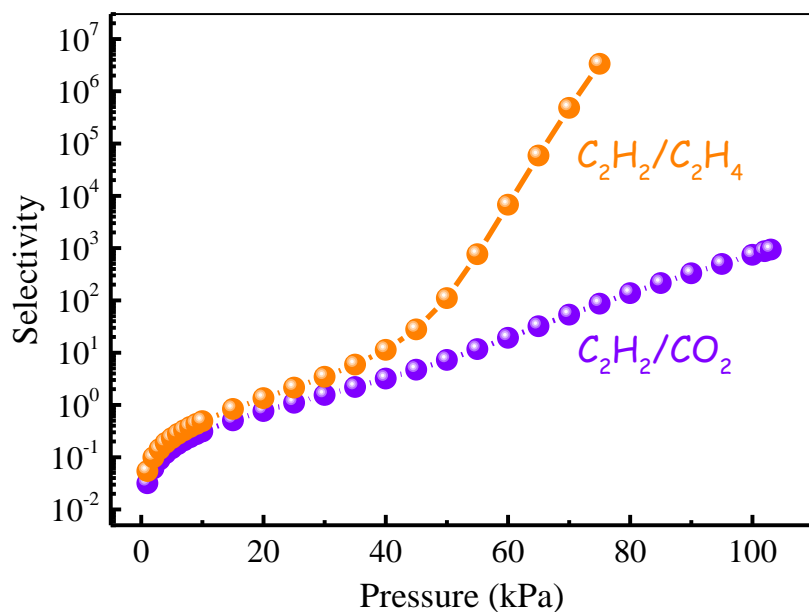


Figure S26. IAST adsorption selectivities of C_2H_2/CO_2 and C_2H_2/C_2H_4 in their equimolar mixtures at 298 K.

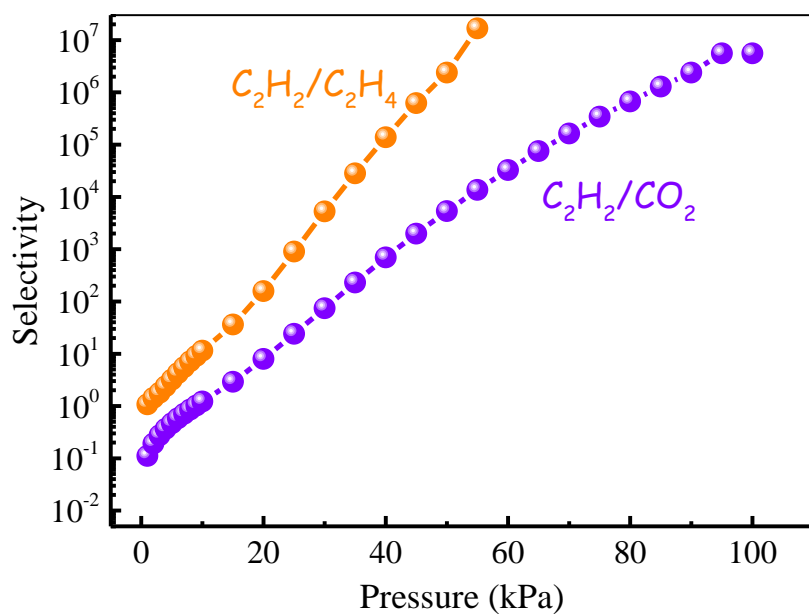


Figure S27. IAST adsorption selectivities of C_2H_2/CO_2 and C_2H_2/C_2H_4 in their equimolar mixtures at 273 K.

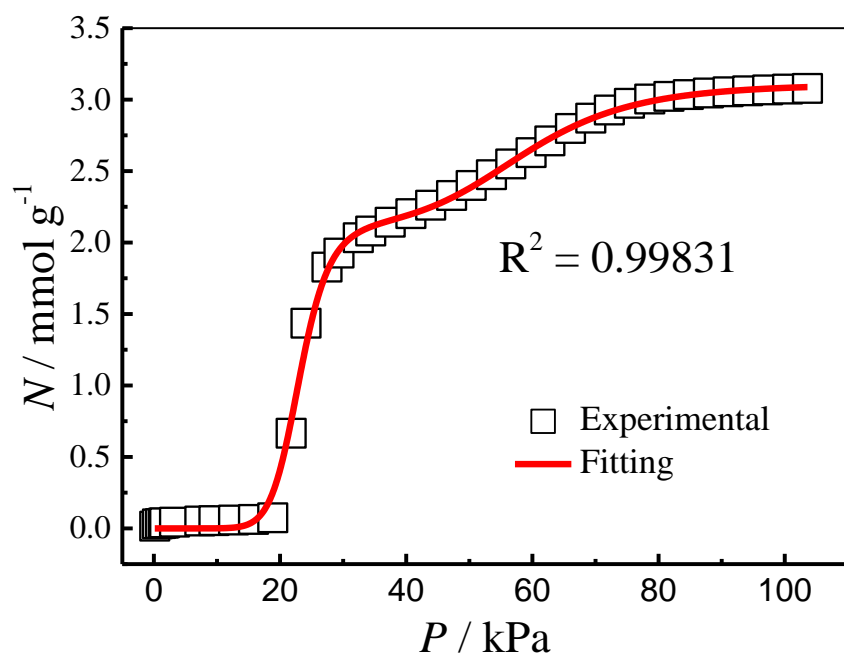


Figure S28. DSLF fitting of the C_2H_2 sorption data at 298 K and 1 bar for UTSA-300a.

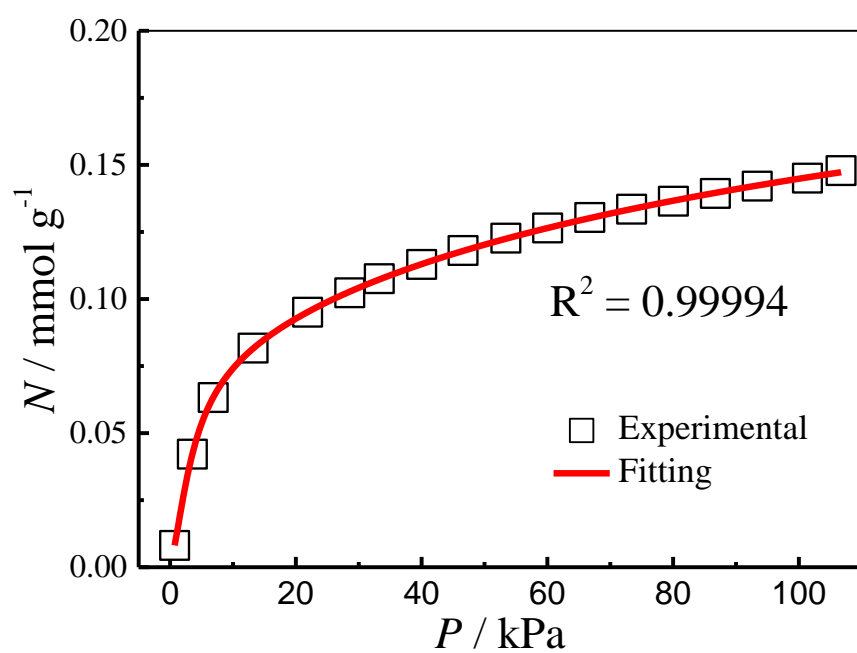


Figure S29. DSLF fitting of the CO_2 sorption data at 298 K and 1 bar for UTSA-300a.

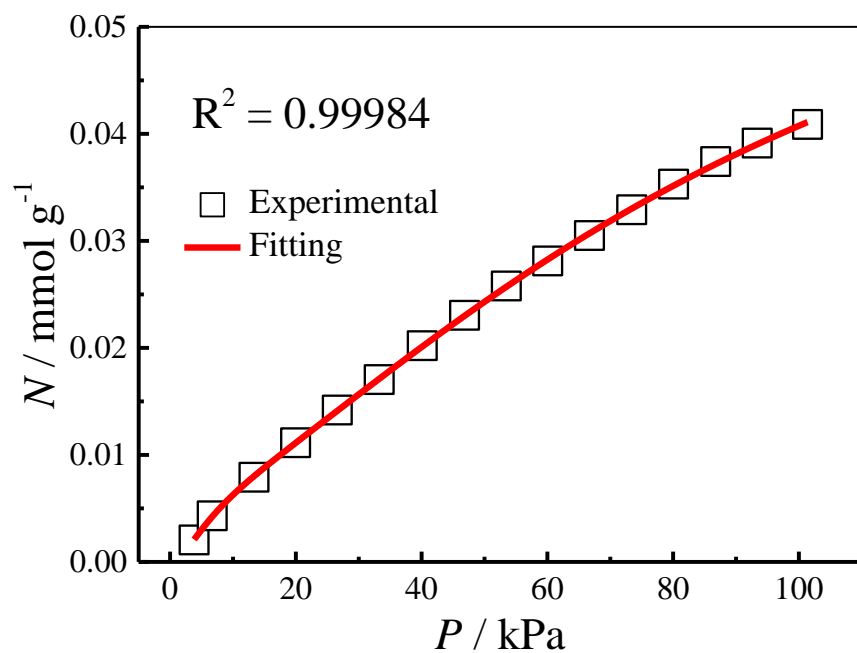


Figure S30. DSLF fitting of the C_2H_4 sorption data at 298 K and 1 bar for UTSA-300a.

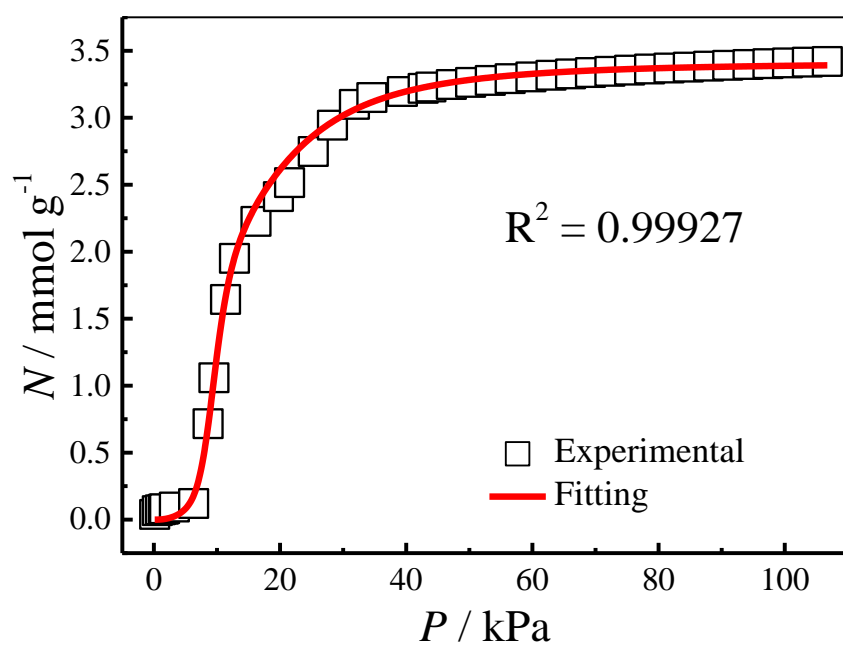


Figure S31. DSLF fitting of the C_2H_2 sorption data at 273 K and 1 bar for UTSA-300a.

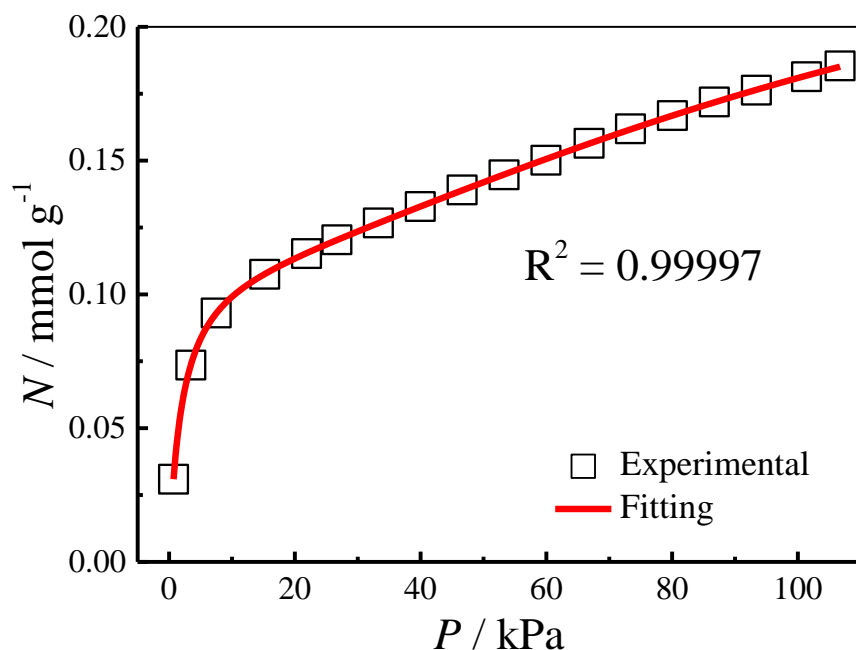


Figure S32. DSLF fitting of the CO₂ sorption data at 273 K and 1 bar for UTSA-300a.

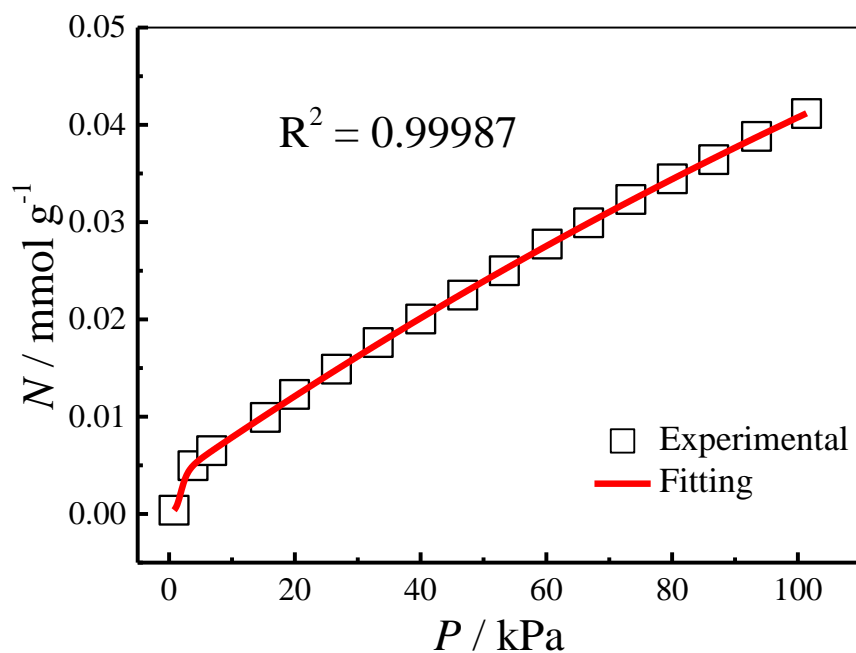


Figure S33. DSLF fitting of the C₂H₄ sorption data at 273 K and 1 bar for UTSA-300a.

Breakthrough separation experiments and procedures

The breakthrough experiments were carried out in dynamic gas breakthrough set-up.^{S2-S4} A stainless steel column with inner dimensions of $\phi 4 \times 150$ mm was used for sample packing. Microcrystalline sample (2.499 g) with particle size of 220–320 μm (Figure S34) obtained via sieving was then packed into the column. The column was placed in a temperature controlled environment (maintained at 273 or 298 K).

The mixed gas flow and pressure were controlled by using a pressure controller valve and a mass flow controller (Figure S35). Outlet effluent from the column was continuously monitored using gas chromatography (GC-2014, SHIMADZU) with a thermal conductivity detector (TCD). The column packed with sample was firstly purged with He flow (100 mL min^{-1}) for 6 h at room temperature 298 K. The mixed gas flow rate during breakthrough process is 2 or 6 mL min^{-1} using 50/50 (v/v) $\text{C}_2\text{H}_2/\text{CO}_2$ and $\text{C}_2\text{H}_2/\text{C}_2\text{H}_4$. After the breakthrough experiment, the sample was regenerated under vacuum.



Figure S34. As synthesized microcrystalline sample for the breakthrough experiments.

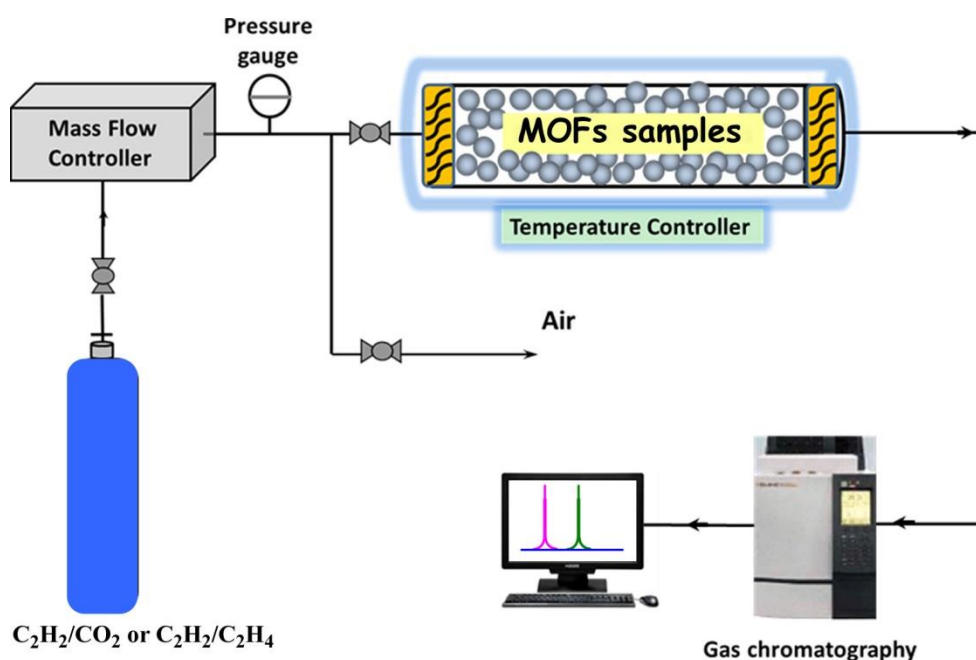


Figure S35. Schematic illustration of the apparatus for the breakthrough experiments.

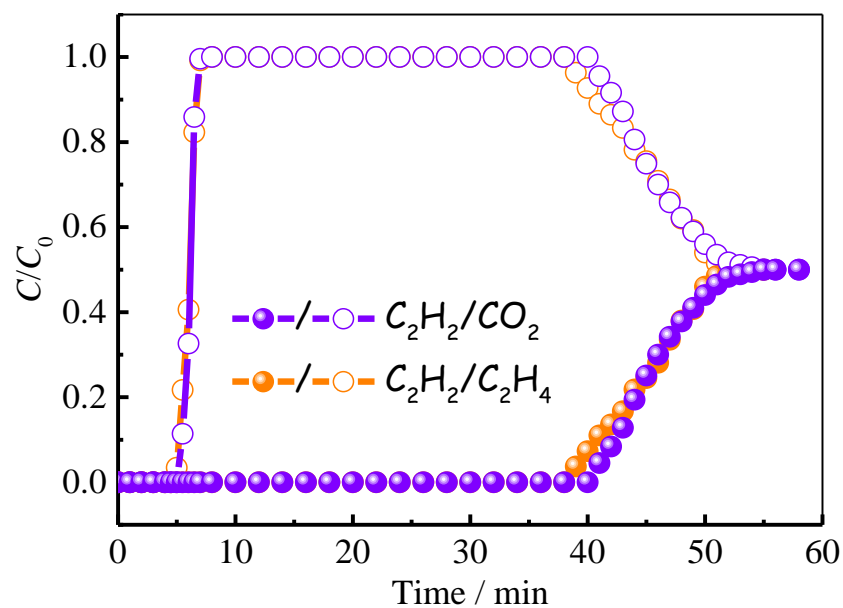


Figure S36. Experimental column breakthrough curves for equimolar C_2H_2/CO_2 (purple) and C_2H_2/C_2H_4 (orange) mixtures (273 K, 1 bar, gas flow: 2 mL/min) in an adsorber bed packed with **UTSA-300a**.

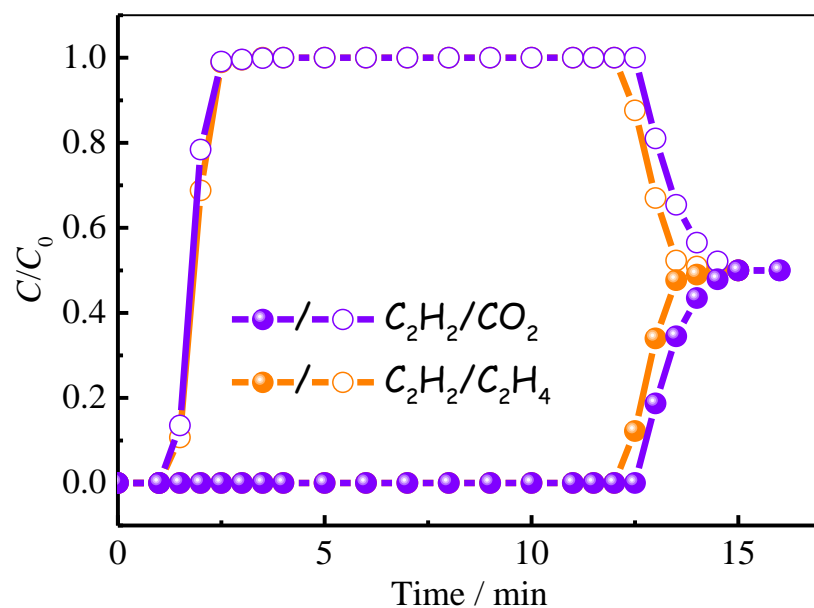


Figure S37. Experimental column breakthrough curves for equimolar C_2H_2/CO_2 (purple) and C_2H_2/C_2H_4 (orange) mixtures (298 K, 1 bar, gas flow: 6 mL/min) in an adsorber bed packed with **UTSA-300a**.

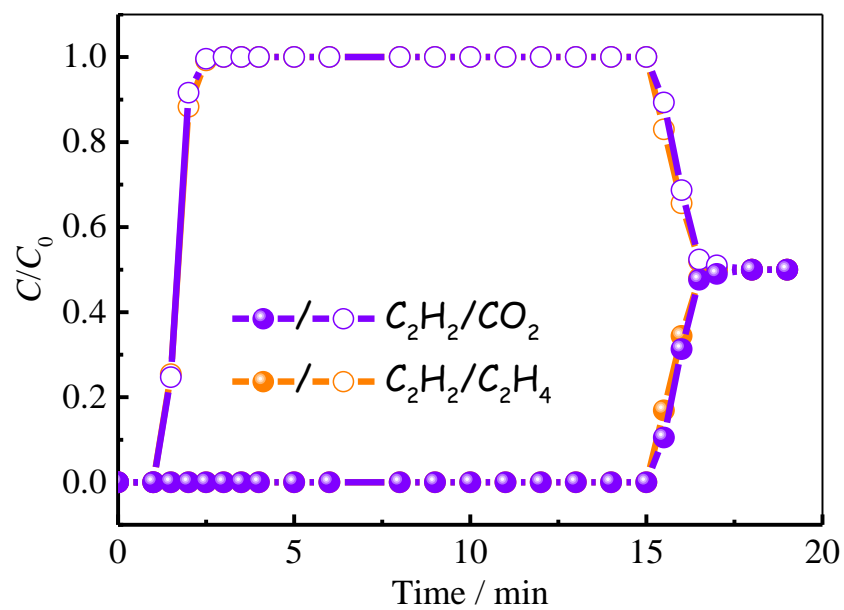


Figure S38. Experimental column breakthrough curves for equimolar C_2H_2/CO_2 (purple) and C_2H_2/C_2H_4 (orange) mixtures (273 K, 1 bar, gas flow: 6 mL/min) in an adsorber bed packed with **UTSA-300a**.

Table S1. Crystal data and structure refinements of **UTSA-300 \supset H₂O**, **UTSA-300a** and **UTSA-300 \supset C₂D₂**.

Complex	UTSA-300 \supset H ₂ O	UTSA-300a	UTSA-300 \supset C ₂ D ₂
Formula.	C ₂₀ H ₁₆ F ₆ N ₄ O ₆ S ₂ SiZn	C ₂₀ H ₁₆ F ₆ N ₄ S ₂ SiZn	C _{23.57} H ₁₆ D _{3.57} F ₆ N ₄ S ₂ SiZn
F.W.	679.99	583.95	634.00
Crystal system	Orthorhombic	Monoclinic	Orthorhombic
Space group	<i>Ibam</i>	<i>P2/n</i>	<i>Ibam</i>
<i>a</i> / Å	10.092(4)	10.1521(8)	10.1705(9)
<i>b</i> / Å	19.277(8)	7.6071(7)	19.358(2)
<i>c</i> / Å	15.171(6)	16.7738(24)	15.272(1)
α /°	90	90	90
β /°	90	102.987(11)	90
γ /°	90	90	90
volume/Å ³	2951(2)	1262.3(3)	3006.8(6)
<i>Z</i>	4	2	4
<i>D</i> _{calc} /g cm ⁻³	1.530	1.562	1.401
μ / mm ⁻¹	1.092	/	/
<i>F</i> 000	1368	/	/
<i>R</i> ₁ ^a <i>I</i> > 2 θ	0.0891	<i>R</i> _p ^c = 0.0162	<i>R</i> _p ^c = 0.0146
<i>wR</i> ₂ ^b <i>I</i> > 2 θ	0.2062	<i>R</i> _{wp} ^d = 0.0193	<i>R</i> _{wp} ^d = 0.0172
<i>R</i> ₁ ^a (all data)	0.0969	/	/
<i>wR</i> ₂ ^b (all data)	0.2116	/	/
GOF	1.167	/	/

$$^a R_1 = \Sigma |F_o - |F_c|| / \Sigma |F_o|, \quad ^b R_{w2} = [\Sigma w(F_o^2 - F_c^2)^2 / \Sigma w(F_o^2)^2]^{1/2}.$$

$$^c R_p = \Sigma |cY^{\text{sim}}(2\theta_i) - I^{\text{exp}}(2\theta_i) + Y^{\text{back}}(2\theta_i)| / \Sigma |I^{\text{exp}}(2\theta_i)|.$$

$$^d R_{wp} = \{w_p[cY^{\text{sim}}(2\theta_i) - I^{\text{exp}}(2\theta_i) + Y^{\text{back}}(2\theta_i)]^2 / \Sigma w_p[I^{\text{exp}}(2\theta_i)]^2\}^{1/2}, \text{ and } w_p = 1/I^{\text{exp}}(2\theta_i).$$

Table S2. Summary of the adsorption uptakes, selectivities and heat of adsorption data for C₂H₂, CO₂ and C₂H₄ in various MOFs (reorganized from ref S11-S13).

MOFs	C ₂ H ₂ (cm ³ /g, STP)	CO ₂ (cm ³ /g, STP)	C ₂ H ₄ (cm ³ / g STP)	V _{C₂H₂} /V _{CO₂}	V _{C₂H₂} /V _{C₂H₄}	Condition	Ref
[Cu ₂ (pzdc) ₂ (pyz)]	42	4	/	10.5	/	270 K, 4.5 kPa	S5
MAF-2	70	19	/	3.68	/	298 K, 100 kPa	S6
HKUST-1	201	113	/	1.78	/	~298 K, 100 kPa	S7
Mg(HCOO) ₂	66	45	/	1.47	/	298 K, 100 kPa	S8
UTSA-74-Zn	108.2	70.9	/	1.53	/	296 K, 100 kPa	S9
[Mn ₃ (bpy) ₃][Mn(CN) ₆] ₂	71	/	5.4	/	13.3	283 K, 100 kPa	S10
M' MOF-3a	42.6	/	9.0	/	4.73	296 K, 100 kPa	S11
SIFSIX-1-Cu	190.4	107.9	92.1	1.74	2.07	298 K, 100 kPa	S12
SIFSIX-2-Cu-i	90.0	108.4	49.1	1.21	1.84	298 K, 100 kPa	S12
SIFSIX-3-Zn	81.5	57.0	50.2	1.43	1.62	298 K, 100 kPa	S12
UTSA-100a	95.6	/	37.2	/	2.57	296 K, 100 kPa	S11
NOTT-300	142	/	95.9	/	1.48	293 K, 100 kPa	S11
MOF-74-Co	183	/	157	/	1.16	296 K, 100 kPa	S11
[Mn(bdc)(dpe)]	7.3	46.8	/	0.156	/	273K, 91 kPa	S13
MOF-74-Fe	152.3	/	136.6	/	1.11	313 K, 100 kPa	S11
UTSA-300a	68.9	3.25	0.92	21	75	298 K, 100 kPa	This
	76.5	4.06	0.92	19	83	273K, 100 kPa	work

Table S3. Equation parameters for the DSLF isotherm model.

Adsorbates	N_1^{\max} (mmol/g)	b_1 (kPa ⁻¹)	$1/n_1$	N_2^{\max} (mmol/g)	b_2 (kPa ⁻¹)	$1/n_2$
UTSA-300a						
C ₂ H ₂ (273 K)	1.57132	2.68341E-8	7.67816	1.84047	7.07776E-4	2.51459
CO ₂ (273 K)	0.11806	0.49533	0.96151	0.15062	3.28404E-4	1.68553
C ₂ H ₄ (273 K)	0.00357	0.04567	4.27267	0.19369	0.00218	1.01872
C ₂ H ₂ (298 K)	2.124	3.82688E-14	9.83515	0.98607	2.07481E-12	6.6095
CO ₂ (298 K)	0.05292	0.11784	1.76735	0.21584	0.02958	0.70021
C ₂ H ₄ (298 K)	0.06618	0.001	1.52186	0.00603	0.02878	1.87926

Reference:

- (S1) Bhattacharya, S.; Gubbins, K. E. *Langmuir* **2006**, 22, 7726.
- (S2) Li, L.; Krishna, R.; Wang, Y.; Yang, J.; Wang, X.; Li, J. *J. Mater. Chem. A*, **2016**, 4, 751.
- (S3) Li, L.; Krishna, R.; Wang, Y.; Wang, X.; Yang, J.; Li, J. *Eur. J. Inorg. Chem.*, **2016**, 4457.
- (S4) Li, L.; Wang, Y.; Yang, J.; Wang, X.; Li, J. *J. Mater. Chem. A*, **2015**, 3, 22574.
- (S5) Matsuda, R.; Kitaura, R.; Kitagawa, S.; Kubota, Y.; Belosludov, R. V.; Kobayashi, T. C.; Sakamoto, H.; Chiba, T.; Takata, M.; Kawazoe, Y.; Mita, Y. *Nature* **2005**, 436, 238.
- (S6) Zhang, J.-P.; Chen, X.-M. *J. Am. Chem. Soc.* **2009**, 131, 5516.
- (S7) Fischer, M.; Hoffmann, F.; Fröba, M. *ChemPhysChem* **2010**, 11, 2220.
- (S8) Kim, H.; Samsonenko, D. G.; Yoon, M.; Yoon, J. W.; Hwang, Y. K.; Chang, J.-S.; Kim, K. *Chem. Comm.* **2008**, 4697.
- (S9) Luo, F.; Yan, C.; Dang, L.; Krishna, R.; Zhou, W.; Wu, H.; Dong, X.; Han, Y.; Hu, T.-L.; O’Keeffe, M.; Wang, L.; Luo, M.; Lin, R.-B.; Chen, B. *J. Am. Chem. Soc.* **2016**, 138, 5678.
- (S10) Hazra, A.; Jana, S.; Bonakala, S.; Balasubramanian, S.; Maji, T. K. *Chem. Commun.* **2017**, 53, 4907.
- (S11) Hu, T.-L.; Wang, H.; Li, B.; Krishna, R.; Wu, H.; Zhou, W.; Zhao, Y.; Han, Y.; Wang, X.; Zhu, W.; Yao, Z.; Xiang, S.; Chen, B. *Nat. Commun.* **2015**, 6, 7328.
- (S12) Cui, X.; Chen, K.; Xing, H.; Yang, Q.; Krishna, R.; Bao, Z.; Wu, H.; Zhou, W.; Dong, X.; Han, Y.; Li, B.; Ren, Q.; Zaworotko, M. J.; Chen, B. *Science* **2016**, 353, 141.
- (S13) Foo, M. L.; Matsuda, R.; Hijikata, Y.; Krishna, R.; Sato, H.; Horike, S.; Hori, A.; Duan, J.; Sato, Y.; Kubota, Y.; Takata, M.; Kitagawa, S. *J. Am. Chem. Soc.* **2016**, 138, 3022.